Modeling near-barrier collisions of heavy ions based on a Langevin-type approach

A. V. Karpov[*] and V. V. Saiko

Flerov Laboratory of Nuclear Reactions, JINR, 141980 Dubna, Russia
and Dubna State University, 141982 Dubna, Russia

Background: Multinucleon transfer in low-energy nucleus-nucleus collisions is proposed as a method of production of yet-unknown neutron-rich nuclei hardly reachable by other methods.

Purpose: Modeling of dynamics of nuclear reactions induced by heavy ions in their full complexity of competing reaction channels remains to be a challenging task. The work is aimed at development of such a model and its application to the analysis of multinucleon transfer in deep inelastic collisions of heavy ions leading, in particular, to formation of neutron-rich isotopes in the vicinity of the $N = 126$ shell closure.

Method: Multidimensional dynamical model of nucleus-nucleus collisions based on the Langevin equations has been proposed. It is combined with a statistical model for simulation of de-excitation of primary reaction fragments. The model provides a continuous description of the system evolution starting from the well-separated target and projectile in the entrance channel of the reaction up to the formation of final reaction products.

Results: A rather complete set of experimental data available for reactions ^{136}Xe + ^{198}Pt, ^{208}Pb, ^{209}Bi was analyzed within the developed model. The model parameters have been determined. The calculated energy, mass, charge, and angular distributions of reaction products, their various correlations as well as cross sections for production of specific isotopes agree well with the data. On this basis, optimal experimental conditions for synthesizing the neutron-rich nuclei in the vicinity of the $N = 126$ shell were formulated and the corresponding cross sections were predicted.

Conclusions: The production yields of neutron-rich nuclei with $N = 126$ weakly depend on the incident energy. At the same time, the corresponding angular distributions are strongly energy dependent. They are peaked at grazing angles for larger energies and extend up to the forward angles at low near-barrier collision energies. The corresponding cross sections exceed 100 nb for the nuclei located at the border of the known region, which is nearly five orders of magnitude larger than can be reached in the fragmentation reactions.

I. MOTIVATION

Production and study of neutron-rich nuclei remains one of the main trends in nuclear physics. A number of facilities work on this subject in the world. One of the main interests here is detailed understanding of the astrophysical r process which proceeds via neutron-rich nuclei far away from the β-stability line. Such nuclei located in the vicinity of the closed neutron shells form the so-called r-process waiting points. Knowing the properties of these nuclides plays a key role in modeling of the r process.

One of the least explored neutron-rich regions of the nuclear chart is that close to the $N = 126$ shell closure. It is due to the low values of the fragmentation cross sections–the only method of production of neutron-rich nuclei in this area used so far. During the last decade three to four new nuclides have been added to each of the isotonic chains in the vicinity of $N = 126$ by ^{238}U and ^{208}Pb fragmentation. The most neutron-enriched nucleus with $N = 126$ known at present, ^{202}Os, was produced [1,2] with the cross section 4.4 ± 2.0 pb [2]. Moreover, only the lower limit of the ^{202}Os half-life was determined. Since the fragmentation cross sections decrease rapidly with each step in the direction on neutron excess, alternative efficient methods of production of these nuclei should be considered.

Multinucleon transfer in the processes of deep inelastic (DI) collisions of heavy ions at near-barrier energies has been considered to be an appropriate method since the discovery of this type of nuclear reactions in 1966 by Volkov and collaborators [3]. A few years later, a number of light neutron-rich nuclei were produced for the first time in DI collisions of light ions with heavy targets (see, e.g., Ref. [4] and references therein). An important feature of DI collisions known as the ground-ground systematics has been revealed already in the early years of study of the DI reactions. It justified the decisive role played by the potential energy of a heavy nuclear system in the dynamics of multinucleon transfer reactions. The cross sections for production of light nuclei were found to be exponentially dependent on the Q value for the ground-state–to–ground-state transfer.

A recently renewed interest in the DI processes is caused, in part, by a widely discussed possibility of synthesizing the unknown neutron-rich isotopes of medium-mass, heavy, and superheavy nuclei [5–10]. A number of experimental studies have already been performed [11–15] aimed at the validation of this idea and studying the peculiarities of the multinucleon transfer reactions in this mass region.

A possibility of synthesis of yet-unknown neutron-rich nuclides around the $N = 126$ neutron shell with quite large cross sections was predicted in Refs. [8,9]. One of the proposed projectile-target combinations is ^{136}Xe + ^{208}Pb. The Q values for proton transfer from lead to xenon are quite small for

this reaction making it favorable according to the ground-ground systematics. The nucleon transfer cross sections were calculated in Refs. [8,9] within a semiclassical dynamical approach based on the Langevin equations. However, the model used in Refs. [8,9], in spite of its success in description of various aspects of nuclear dynamics (including synthesis of superheavy nuclei), usually quite strongly underestimates the multinucleon transfer cross sections when the nucleon transfer leads to the system antisymmetrization (see, e.g., Fig. 6 of Ref. [11])—the proposed way of synthesis of neutron-rich isotopes of heavy and superheavy elements. Thus, the primary purpose of this work is developing a model suitable for the analysis of near-barrier collisions of heavy ions in the whole range of masses, charges, energies, and scattering angles of the reaction products.

There are several theoretical approaches used at present for analysis of such a complicated process as a collision of two heavy nuclei. One of them is the already mentioned Langevin-equations-based approach, discussed in detail in the following section. A number of versions of this approach were elaborated (see, e.g., Refs. [16–19]). All these models differ in the number of included collective degrees of freedom, the potential energy governing the system evolution, transport coefficients, initial and boundary conditions, etc. These model "ingredients" determine its applicability to different types of nuclear reactions. For example, the model [19] was never applied to the analysis of fusion-fission reactions, since the necking degree of freedom was not included in the model. In contrast, the model [17] was shown to work well for fusion-fission and quasifission reactions, but the first (approaching) stage of the reaction is considered within the coupled-channel model [20] and the initial conditions for the Langevin model are formulated at the point of contact of two nuclei, where they are quite uncertain.

A rather widely used approach to the description of low-energy nucleus-nucleus collisions is the so-called dinuclear system model [4,10,21–23]. This model is based on the assumption that the nuclear dynamics is regulated by the diabatic nucleus-nucleus potential. After the contact, nuclei stop at the bottom of the potential and the further evolution in the elongation degree of freedom towards compact shapes of the compound nucleus (CN) is prohibited due to the repulsive at short distances potential. The CN formation is assumed to proceed via the nucleon transfer from the lighter nucleus to the heavier one until its complete "melting."

Another type of approach employed for modeling nuclear dynamics is an (improved) quantum molecular dynamics model [24–27]. Within this approach, each nucleon of a system is represented as a wave packet. Its propagation in time is governed by the self-consistently generated mean field entering Hamiltonian equations for the center of the wave packet in coordinate and momentum space. In spite of a recent successful effort made for developing this model, there are still significant difficulties. The shell effects, responsible, in particular, for the existence of nuclei deformed in their ground states, are not yet fully included in the model. As a result, the nuclei in the initial state are spherical which constrains the model applicability to the collisions of statically deformed nuclei.

Probably the most impressive progress in understanding the dynamics of nucleus-nucleus collisions was made in recent years within the time-dependent Hartree-Fock (TDHF) approach [28–32]. At the same time, the TDHF approach is a deterministic one, suffering from the absence of dissipative effects originating from the interaction of collective and single-particle subsystems. As a result, it describes the time evolution of the dominant reaction channel, rather than the competition of multiple reaction channels. In order to overcome this problem one should go beyond the mean-field theory (see, e.g., recent review [33] and references therein).

A semiclassical approach based on the Langevin equations remains to be a powerful tool for analysis of low-energy nucleus-nucleus collisions allowing one to model low-energy collisions of heavy ions in their complexity of competing reaction channels. This paper is aimed at developing such a model, determining its adjustable parameters, and analyzing available experimental data for reactions ^{136}Xe + ^{198}Pt, ^{208}Pb, ^{209}Bi. Finally, the optimal conditions for production of neutron-rich nuclei with $N = 126$ in these reactions are discussed.

II. MODEL

The model developed in this work is based on the same principles as the one of Zagrebaev and Greiner [8,19] and can be considered as its extension or generalization. Since the model of Refs. [8,19] and its predictions are widely known, we list here its most important (but not all) differences with the present one. The details on each of the points will be given below.

Degrees of freedom. Independent deformations of a target and a projectile are used in the present work instead of a single deformation degree of freedom for the whole system in the model [8,19]. A neck degree of freedom is included in this model, which is important for all damped collisions but especially for the fusion-fission reactions (not considered in this work).

Potential energy. The potential energy is calculated in our model within a two-center shell model, whereas in the model [8,19] its approximation, a so-called two-core model, was employed.

Equations of motion. Instead of the inertialess reduced Langevin equations for mass and charge asymmetries, we solve the full Langevin equations including also mass and charge fluctuations of yet unexcited nuclei in the entrance channel. This allowed us to solve the above-mentioned problem with the description of mass transfer leading to the system antisymmetrization.

Transport coefficients. We use full inertia and friction tensors including the off-diagonal terms, whereas the tensors were assumed to be diagonal in the model [8,19]. The friction tensor is calculated in the present model within a one-body dissipation model which was shown (see, e.g., the corresponding discussions in Ref. [34]) to work better for the fusion-fission reactions, rather than a two-body one as used in the model [8,19].

A near-barrier collision of two nuclei may be described as a sequence of several main stages:

  (i) *Approaching stage.* The interaction of two nuclei, initially being in their ground states, increases as

the distance between their centers is getting shorter. Already at this stage, deformations of the reaction partners are not any more the ground-state ones. The evolution of the deformation degrees of freedom starts quite early due to a shift of an optimal deformation (providing minimum of the potential energy) towards more prolate shapes of the interacting nuclei. The next important feature of this stage is the possibility of nucleon transfer even before the nuclei come into the contact. It was shown in several works that already at the approaching stage of nucleus-nucleus collisions the wave function of a valence neutron (localized initially in one of the nuclei) may spread into the volume of another nucleus (see, e.g., Refs. [28,29,35,36]) *before* the colliding nuclei have overcome the Coulomb barrier. Finally, interaction of statically deformed nuclei, i.e., deformed in their ground states, depends strongly on the angles of mutual orientation, which should be taken into account. Note that in this paper the reactions between nuclei having zero ground-state deformations are analyzed.

 (ii) *Formation of a mononucleus and its evolution.* Strong dissipation of the kinetic energy of the relative motion into the excitation energy starts at the end of the approaching stage, when diffusenesses of nuclear matter distributions overlap. Thus, after the contact, an excited mononucleus is formed. Its evolution is governed mainly by the peculiarities of the landscape of the potential energy surface and interplay between nuclear friction forces determining the transformation of the kinetic energy of collective motion into the internal excitation, on the one hand, and thermal fluctuations of the collective degrees of freedom due to coupling of the internal and collective subsystems on the other. At this stage, a substantial change of the mononucleus shape may occur, resulting, first of all, in an intensive nucleon transfer between the two parts of the system as well as their large deformations. The system parts may even totally lose their individualities and form a compound nucleus. Finally, the system decays and forms either a cold evaporation residue or two fragments.

 (iii) *Formation of reaction fragments.* Separation of the system into two fragments (neck rupture) terminates the nucleon exchange and energy dissipation processes. Masses and charges of the primary fragments are now fixed. The fragments accelerate in the field of their interaction. An extra deformation of the fragments existing at the moment of scission gradually disappears. The corresponding deformation energy transforms into the fragments' excitation. Thus, two primary excited fragments are formed. Their de-excitation may proceed either by particle evaporation (mainly neutrons, protons, α particles, and γ quanta) or sequential fission process.

A. Degrees of freedom

Due to a competition and substantial overlapping of heavy-ion reaction channels, a unified dynamical approach for the
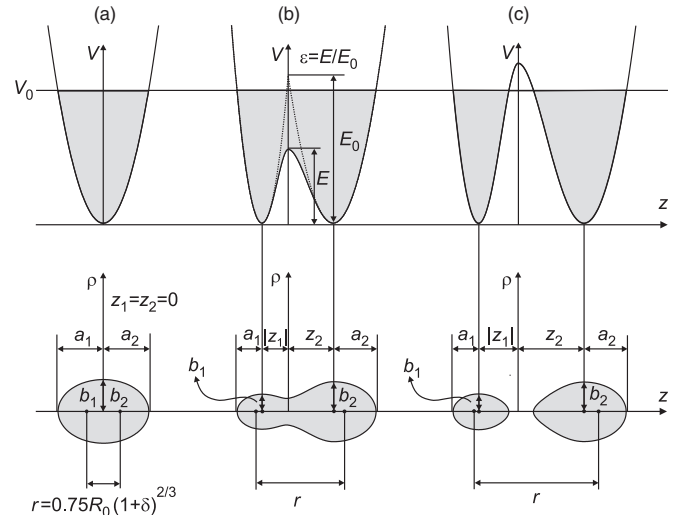
FIG. 1. Example of the nuclear shapes in two-center parametrization and the corresponding potentials $V(\rho = 0, z)$ shown for $\delta_1 = \delta_2 = 0.5$ and $\varepsilon = 0.5$. The mass asymmetry $\eta = 0$ for (a) and $\eta = 0.625$ for (b) and (c).

simultaneous description of all the possible processes is needed. The model should have a unified set of degrees of freedom playing the most important role at all the stages of the process. The choice of these degrees of freedom is the first step on the way of development of such a model. Their number should be large enough to reproduce the main features of the process of the nucleus-nucleus collision and simultaneously describe the strongly overlapping reaction channels. At the same time, we are limited by the present computational possibilities.

The parametrization originating from the well-known two-center shell model (TCSM) [37–41] is used to describe the shape of the system. Some basic details of the TCSM are given in Sec. II B. More detailed information can be found, e.g., in Ref. [42]. The profile function determining an axially symmetric nuclear shape in cylindrical coordinates has the form

$$
\rho_s^2(z) = \begin{cases} b_1^2 \left[1 - \frac{z'^2}{a_1^2}\right], & z \leqslant z_1, \\ b_1^2 \left[1 - \frac{z'^2}{a_1^2}(1 + c_1 z' + d_1 z'^2)\right]\frac{1}{(1+g_1 z'^2)}, \\ z_1 < z < 0, \\ b_2^2 \left[1 - \frac{z'^2}{a_2^2}(1 + c_2 z' + d_2 z'^2)\right]\frac{1}{(1+g_2 z'^2)}, \\ 0 < z < z_2, \\ b_2^2 \left[1 - \frac{z'^2}{a_2^2}\right], & z \geqslant z_2, \end{cases} \tag{1}
$$

where

$$
z' = \begin{cases} z - z_1, & z \leqslant 0, \\ z - z_2, & z > 0. \end{cases} \tag{2}
$$

We readily see (Fig. 1) that the external, with respect to the oscillator centers z_1 and z_2, parts of the shape are axially symmetric ellipsoids centered at z_i with semiaxes a_i and b_i ($i = 1,2$). The internal part of the shape is more complicated. The shape parametrization has 12 free parameters (z_i, a_i, b_i, c_i, d_i, and g_i), seven of which can be fixed from the conditions of volume conservation and continuity of the profile function and

its derivative at the matching point $z = 0$. Therefore, the shape parametrization of the TCSM has five independent parameters, that allow us to introduce five collective variables:

(1) The distance between the oscillator centers (elongation) $r = z_2 - z_1$, which for separated nuclei is approximately the distance between centers of masses of the nuclei.

(2),(3) Two independent ellipsoidal deformations δ_1 and δ_2 of the two parts of the system, defined as $\delta_i = a_i/b_i - 1$.

(4) The mass asymmetry $\eta_A = (A_2 - A_1)/(A_1 + A_2)$, where A_1 and A_2 are the masses (volumes) of the left ($z < 0$) and right ($z \geqslant 0$) parts of the system, respectively.

(5) The neck parameter ε. It originates from the shape smoothing between the centers z_i. The smaller ε is, the thicker the neck is at fixed values of the other parameters. It is clear that the difference between the entrance- and the exit-channel (especially fission) shapes should be taken into account. It is usually supposed that nuclear shapes corresponding to scission configurations in the fission channel are characterized by a large distance between centers of mass and a well pronounced neck. On the contrary, the shapes at the contact point in the fusion channel are rather compact and almost neckless. These shapes can be described well with $\varepsilon = 1$. For the exit (fission) channel the value of the neck parameter should minimize the potential energy along the fission path. The value $\varepsilon \approx 0.35$ was recommended in Ref. [43] for the fission process. In order to reduce the number of independent variables, we use an approximate treatment of the neck parameter suggested in Ref. [42]. The time evolution of the neck parameter is considered as a relaxation process with the characteristic time τ_ϵ.

Thus, the model has four degrees of freedom (r, δ_1, δ_2, and η_A) determining the shape of the nuclear system. The model also includes the charge asymmetry defined as $\eta_Z = (Z_2 - Z_1)/(Z_2 + Z_1)$, where Z_1 and Z_2 are the charges of the left and right parts of the system, respectively. This degree of freedom is necessary for analysis of transfer reactions with the formation of different isotopes of a given element. Note that the charge asymmetry η_Z changes the ratio of protons in the two parts of the system without changing its shape.

Additionally, two angles φ_i of rotation of the nuclei and the angle θ between the symmetry axis and the beam direction are considered as independent variables. Thus, in total, the model has eight degrees of freedom shown schematically in Fig. 2.

B. Potential energy

The interaction potential of two separated nuclei can be calculated quite easily as a sum of the interaction energy of the nuclei, their deformation energies, and the Q value of the reaction. However, after overcoming the Coulomb barrier and touching of the nuclear surfaces, two different ways of
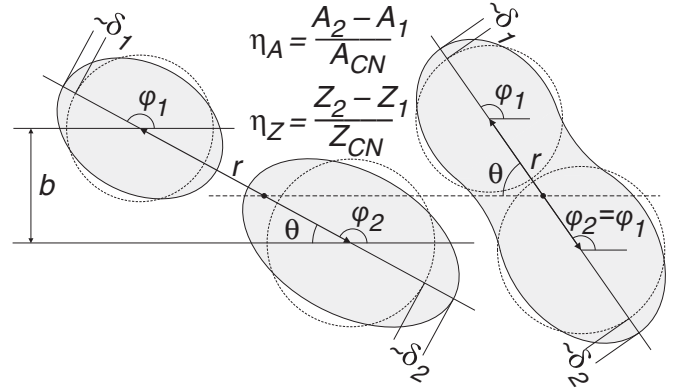
FIG. 2. Schematic view of the nuclear degrees of freedom.

evolution of the nuclear system are possible. The diabatic regime (or so-called condition of "frozen nuclei") takes place when the approaching velocity v_{rel} of two nuclei is higher than the velocity v_F of Fermi motion of nucleons $v_{\text{rel}} > v_F$. In this case, after the contact, the nuclei may penetrate into each other keeping their shapes. This leads to doubling of the nuclear density and, finally, to the appearance of the repulsive core in the potential energy, preventing the nuclei from mutual penetration [44,45].

In the case of slow near-barrier collisions, $v_{\text{rel}} \ll v_F$, the system has enough time to change its shape and single-particle levels and keep nuclear density constant (adiabatic condition), which minimizes the potential energy. The adiabatic potential energy noticeably differs from the diabatic one for the elongations smaller than the contact configuration $r < R_{\text{contact}}$. At the same time, these potentials must coincide for well separated nuclei.

Thus, for the nucleus-nucleus collisions at energies well above the Coulomb barrier we use a time-dependent potential energy, which is gradually transformed from the diabatic potential energy into the adiabatic one, when the target and the projectile approach at the distance of nuclear interaction [19,46]

$$V_{\text{pot}}(A,Z;\vec{q};\tau) = V_{\text{diab}}(A,Z;\vec{q})f(\tau)$$
$$+ V_{\text{adiab}}(A,Z;\vec{q})[1 - f(\tau)], \quad (3)$$

where $\vec{q}$ is a set of collective coordinates used. In Eq. (3), τ is the interaction time and $f(\tau)$ is a smoothing function with parameter τ_{DA}, and the following properties: $f(\tau = 0) = 1$ and $f(\tau \gg \tau_{\text{DA}}) = 0$. We use a rather simple function:

$$f(\tau) = \exp\left(-\frac{\tau}{\tau_{\text{DA}}}\right). \quad (4)$$

The time evolution of the neck degree of freedom ε is considered in the same way as the transition from the diabatic to the adiabatic regime. The entrance and the exit channel potentials are calculated with $\varepsilon = 1$ (no neck) and with $\varepsilon = 0.35$, respectively. The transition time is denoted as τ_ε.

Both the adiabatic and diabatic potentials in Eq. (3) depend on the same collective degrees of freedom. This allows one to consider the collision dynamics continuously, starting from
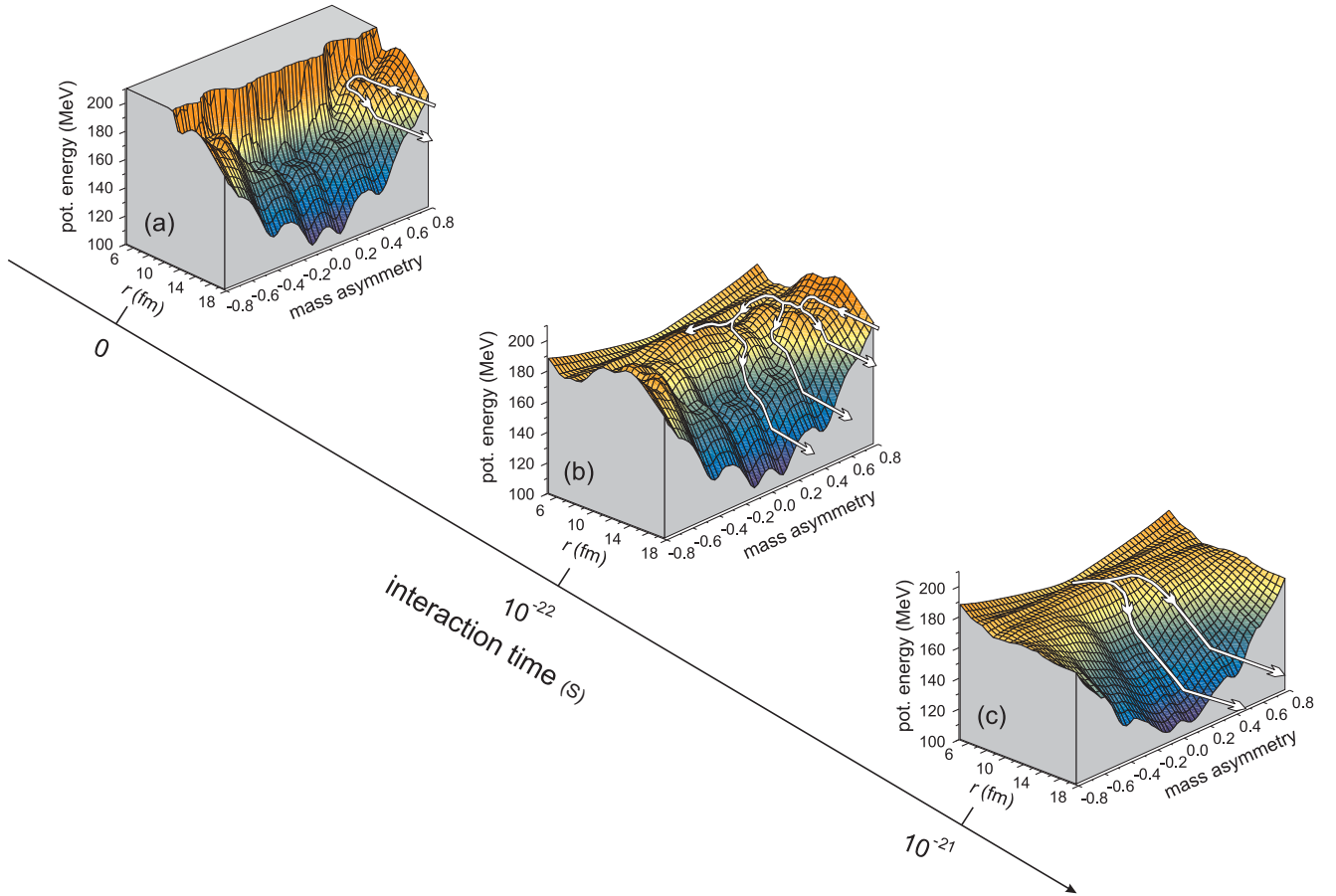
FIG. 3. Time evolution of the potential energy for the ^{48}Ca $+^{248}$Cm system at zero dynamic deformations. (a) The diabatic potential energy calculated using the double-folding procedure (the first stage). The entrance-channel (b) and fission-channel (c) adiabatic potential energies obtained within the extended macro-microscopic approach. The white arrows schematically show the most probable reaction channels: DI scattering (a); DI scattering, quasifission, and fusion (b); and multimodal fission (c).

the separated target and projectile approaching each other in the entrance channel and up to the formation of final fragments. An example of the time evolution of the potential energy for the ^{48}Ca $+^{248}$Cm system is shown in Fig. 3. The intermediate adiabatic potential without necking [Fig. 3(b)] is not really reached, since the development of the neck degree of freedom and diabatic-adiabatic regime transition proceed simultaneously.

The transition to equilibrium nucleon distribution and, therefore, to the adiabatic regime of motion is rather fast. The characteristic time for the relaxation process is estimated to be $\sim 10^{-22}$–10^{-21} s [46,47]. The relaxation times are the model parameters and can be determined from the analysis of experimental data on DI scattering of nuclei. The determined values $\tau_{DA} = 10^{-22}$ s and $\tau_{\varepsilon} = 10^{-21}$ s are in agreement with the previous estimations.

1. Diabatic potential energy

Redistribution of nucleons between separated nuclei changes their binding energies. It is convenient to include such energy change in the nuclear potential energy. Thus, the diabatic potential energy is defined as follows:

$$
\begin{aligned}
V_{\text{diab}}(A,Z;\vec{q}) = {} & V_{12}(A,Z;\vec{q}) \\
& + M(A_1,Z_1;\delta_1) + M(A_2,Z_2;\delta_2) \\
& - M\big(A_T,Z_T;\delta_T^{\text{g.s.}}\big) - M\big(A_P,Z_P;\delta_P^{\text{g.s.}}\big).
\end{aligned}
\tag{5}
$$

Here V_{12} is the interaction energy of the nuclei, $M(A_i,Z_i;\delta_i)$ $(i = 1,2)$ are the masses of the reaction fragments, and the constant value $M(A_T,Z_T;\delta_T^{\text{g.s.}}) + M(A_P,Z_P;\delta_P^{\text{g.s.}})$ (the sum of the ground-state masses of target and projectile) provides zero value of the potential energy in the entrance channel at infinite distance between the nuclei. It is easy to see that the value of V_{diab} at infinite distance is equal to the Q value of the corresponding reaction.

The key component of the diabatic potential energy is the interaction energy of the nuclei V_{12}. We apply a double-folding procedure to its calculation. The double-folding method consists in summation of the effective nucleon-nucleon interactions (see, e.g., [48]). The effects of deformation and orientation are then taken into account automatically. The

interaction energy of two nuclei is given by

$$V_{12} = \int_{V_1} \rho_1(\mathbf{r}_1) \int_{V_2} \rho_2(\mathbf{r}_2) v_{NN}(\mathbf{r}_{12}) d^3 r_1 \mathrm{d}^3 r_2, \qquad (6)$$

where $v_{NN}(\mathbf{r}_{12} = \mathbf{r} + \mathbf{r}_2 - \mathbf{r}_1)$ is the effective nucleon-nucleon interaction which consists of the Coulomb and the nuclear parts $v_{NN} = v_{NN}^{(N)} + v_{NN}^{(C)}$, and $\rho_i(\mathbf{r}_i)$ are the density distributions of nuclear matter in the nuclei ($i = 1,2$).

The nuclear density is parametrized by the Fermi-type function

$$\rho(\mathbf{r}) = \rho_0 \left[1 + \exp\left(\frac{r - R(\Omega_{\mathbf{r}})}{a} \right) \right]^{-1}, \qquad (7)$$

where $R(\Omega_{\mathbf{r}})$ is the distance to the nuclear surface, $\Omega_{\mathbf{r}}$ are the spherical coordinates of the vector $\mathbf{r}$, and the value ρ_0 is determined from the condition $\int \rho_i \mathrm{d}^3 r = A_i$. There are two independent parameters in this formula: the diffuseness of the nuclear density a and the nuclear radius parameter r_0.

The Coulomb part of the nucleon-nucleon interaction has the form

$$v_{NN}^{(C)}(r) = e^2/r. \qquad (8)$$

Different models can be used for the nuclear part $v_{NN}^{(N)}$. It was suggested in Ref. [49] to use a zero-range nucleon-nucleon potential based on the density-dependent Migdal potential [50], which significantly simplifies the calculation of the sixfold integral in Eq. (6),

$$v_{NN}^{(N)}(\mathbf{r}_1, \mathbf{r}_2) = C \left[F_{\mathrm{ex}} + (F_{\mathrm{in}} - F_{\mathrm{ex}}) \frac{\rho_1(\mathbf{r}_1) + \rho_2(\mathbf{r}_2)}{\rho_{00}} \right] \delta(\mathbf{r}_{12}), \qquad (9)$$

where

$$F_{\mathrm{ex(in)}} = f_{\mathrm{ex(in)}} \pm f'_{\mathrm{ex(in)}}. \qquad (10)$$

The sign "+" corresponds to the interaction of identical particles (proton-proton or neutron-neutron), while the sign "−" is for different particles (proton-neutron). The following values were recommended in Ref. [50] for the fixed value of the normalization constant $C = 300$ MeV fm^3: $f_{\mathrm{in}} = 0.09$; $f_{\mathrm{ex}} = -2.59$; $f'_{\mathrm{in}} = 0.42$; and $f'_{\mathrm{ex}} = 0.54$. The quantity ρ_{00} is the central nuclear density for which we use the mean value of the central densities of the interacting nuclei $\rho_{00} = (\rho_{01} + \rho_{02})/2$. Further details on the use of the Migdal nucleon-nucleon potential for calculation of the diabatic potential can be found in Ref. [42]. The parameters for the nuclear matter distribution were fitted in Ref. [42] to reproduce the fusion barriers. The maximum obtained deviation from the empirical Bass barriers [51] was found to be less than 2 MeV.

2. Adiabatic potential energy

As mentioned above, the adiabatic regime of motion assumes equilibrium nuclear densities. In the vicinity of the contact point, an arbitrarily oriented nuclear system gradually relaxes to the axially symmetric configuration of a mononucleus. Therefore, the adiabatic potential energy is independent of the mutual orientation for the elongations smaller than the contact configuration (in contrast to the diabatic potential). It is well known that the orientation effects

play a very important role in the fusion dynamics decreasing the Coulomb barrier for the nose-to-nose configuration. However, consistent consideration of the transition from the configuration of two arbitrarily oriented deformed nuclei before touching to the axially symmetric mononucleus within the adiabatic approximation requires knowing the successive shapes passed by the system. This is a very complicated problem, which is not solved yet. Usually the axial symmetry is assumed in calculation of the adiabatic potential energy. An approximate treatment of the adiabatic motion for another limit configuration (side to side) was proposed in Ref. [8] within the two-core model.

The adiabatic potential energy is defined as a difference between the mass of the whole nuclear system (the system could be either a mononucleus or two separated nuclei) and the ground-state masses of the target and the projectile,

$$V_{\mathrm{adiab}}(A,Z;\vec{q}) = M(A,Z;\vec{q}) - M\left(A_T, Z_T; \delta_T^{\mathrm{g.s.}}\right) - M\left(A_P, Z_P; \delta_P^{\mathrm{g.s.}}\right). \qquad (11)$$

The last two terms in this expression again provide a zero value of the adiabatic potential energy in the entrance channel for the ground-state deformations of the target and the projectile at infinite distance between them.

The standard macro-microscopic model is often used for calculation of the total mass:

$$M(A,Z;\vec{q}) = M_{\mathrm{mac}}(A,Z;\vec{q}) + \delta E(A,Z;\vec{q}). \qquad (12)$$

Here M_{mac} is the macroscopic liquid-drop mass, and the second term, δE, is the microscopic shell correction which can be calculated using the Strutinsky shell-correction method [52,53].

The macroscopic mass is usually evaluated within a certain version of the liquid-drop model. In particular, we use the finite-range liquid-drop model (FRLDM) [54–56], which gives the macroscopic mass for the uniform charge distribution (i.e., $\eta_Z = \eta_A$). The dependence on the charge asymmetry η_Z can be taken into account as an additional term.

The FRLDM macroscopic mass has the form

$$\begin{aligned}
M_{\mathrm{mac}}&(A,Z;\vec{q})\,|_{\eta_Z = \eta_A} \\
&= m_p Z + m_n N - a_v (1 - k_v I^2) A \\
&\quad + a_s (1 - k_s I^2) B_N(\vec{q}) A^{2/3} + \frac{3}{5} \frac{e^2 Z^2}{r_0 A^{1/3}} B_C(\vec{q}) \\
&\quad - \frac{3}{4} \frac{e^2}{r_0} \left(\frac{9 Z^4}{4\pi^2 A} \right)^{1/3} + f(k_F r_p) \frac{Z^2}{A} - c_a(N - Z) + a_0 \\
&\quad + W \left(|I| + \begin{cases} 1/A, & Z \text{ and } N \text{ equal and odd} \\ 0, & \text{otherwise} \end{cases} \right) \\
&\quad + \begin{cases} \bar{\Delta}_p + \bar{\Delta}_n - \delta_{np}, & Z \text{ and } N \text{ odd} \\ \bar{\Delta}_p, & Z \text{ odd and } N \text{ even} \\ \bar{\Delta}_n, & Z \text{ even and } N \text{ odd} \\ 0, & Z \text{ and } N \text{ even} \end{cases} \\
&\quad - a_{\mathrm{el}} Z^{2.39}. \qquad (13)
\end{aligned}$$

The terms in this formula are respectively the masses of Z protons and N neutrons; the volume energy; the nuclear (surface) and the Coulomb energies depending on deformation via the dimensionless functionals B_N and B_C, respectively; the Coulomb exchange correction; the proton form-factor correction to the Coulomb energy; the charge-asymmetry energy [$(N - Z)$ term]; the constant term; the Wigner energy; the average pairing energy; and the energy of bound electrons.

In order to calculate the macroscopic mass for an arbitrary value of η_Z we use a parabolic approximation of the potential energy dependence on η_Z [57–59],

$$M_{\text{mac}}(A,Z;\vec{q}) \simeq M_{\text{mac}}(A,Z;\vec{q})\mid_{\eta_Z = \langle \eta_Z \rangle}$$
$$+ C_{\eta_Z} \frac{(\eta_Z - \langle \eta_Z \rangle)^2}{2}, \qquad (14)$$

where $\langle \eta_Z \rangle$ is the charge asymmetry providing the minimum of the potential energy and C_{η_Z} is the stiffness coefficient. It is convenient to rewrite the above formula as

$$M_{\text{mac}}(A,Z;\vec{q}) \simeq M_{\text{mac}}(A,Z;\vec{q})\mid_{\eta_Z = \eta_A}$$
$$- C_{\eta_Z} \frac{(\eta_A - \langle \eta_Z \rangle)^2}{2} + C_{\eta_Z} \frac{(\eta_Z - \langle \eta_Z \rangle)^2}{2}, \qquad (15)$$

so the first term can be calculated according to Eq. (13). The quantities $\langle \eta_Z \rangle$ and C_{η_Z} can be defined as follows [57,59]:

$$C_{\eta_Z}(A,Z;\vec{q}) = \frac{2c_s Z_{CN}^2 (1+k)^2}{k A_{CN}} + \frac{(1+k)^2 E_C^0}{2k^2}$$
$$\times \left[(1+k)\left(B_C^1(\vec{q}) + k B_C^2(\vec{q})\right) - k B_C(\vec{q}) \right],$$

$$\langle \eta_Z \rangle (A,Z;\vec{q}) = \frac{(1+k)^2}{2k^2 A_{CN} C_{\eta_Z}} \big\{ 4c_s k Z_{CN}^2 \eta_A + E_C^0 A_{CN}$$
$$\times \left[B_C^1(\vec{q}) - k^2 B_C^2(\vec{q}) \right] \big\}, \qquad (16)$$

where $k = A_1/A_2$ is the mass ratio of the nascent fragments, E_C^0 is the Coulomb energy of the spherical compound nucleus, $B_C^i(\vec{q})$ is the Coulomb energy of the ith nascent fragment, and c_s is the coefficient of the symmetry energy. An example of the potential energy as a function of the atomic and mass numbers is shown in Fig. 4 for the ^{136}Xe + ^{209}Bi system. Two pronounced minima correspond to the strongly bound ^{136}Xe and ^{209}Bi nuclei. The potential forms a valley with very steep walls. This forces the system to evolve mainly along the bottom of the potential (dashed curve) suppressing mass and charge transfers in other directions.

The Strutinsky method [52,53] was applied to calculation of the shell correction. The value of δE is evaluated separately for the neutron and the proton subsystems and includes the microscopic correction to the pairing energy as well. We use the TCSM to calculate the required single-particle spectra. The mean-field potential of the TCSM consists of two potentials of axially symmetric harmonic oscillators with independent centers (Fig. 1). This model is able to describe the transition from the small ellipsoidal deformations near the nucleus ground state, where it coincides with the well-known Nilsson model, to the strongly deformed shape and then to the system of two completely separated nuclei, where it reduces to the Nilsson model for each of the fragments. We use the version of the TCSM developed in Ref. [41], where the model
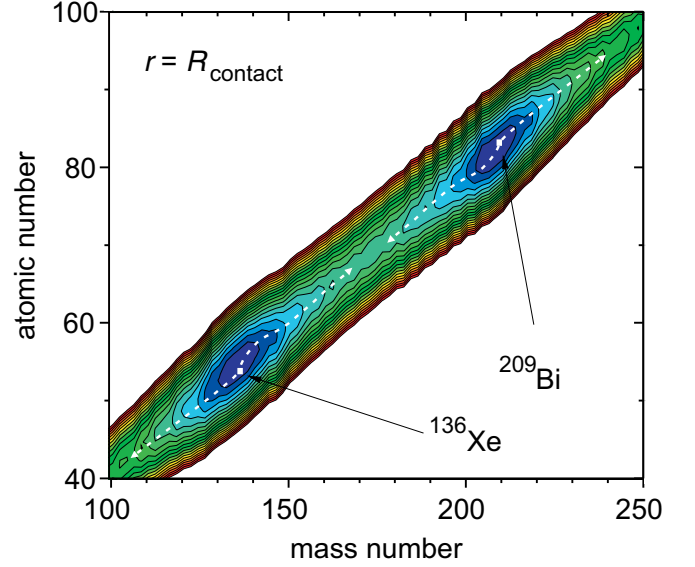
FIG. 4. The potential at the contact point for the ^{136}Xe + ^{209}Bi system calculated at zero values of the deformations. The dashed curve corresponds to the minimum of the potential energy. The contour lines are drawn over each 5 MeV.

was, in particular, extended to the case of mass-asymmetric shapes, and the mean-field potential was modified providing the smooth behavior in the point of the fragments touching.

In spite of a rather good agreement with the experimental ground-state masses and fission barriers, direct application of the standard macro-microscopic approach and, in particular, expression (13) to the case of highly deformed mononucleus and/or two separated nuclei leads to an incorrect result [42]. The main reason for this consists in nonadditivity of Eq. (13) with respect to A and Z. In particular, the standard formula for macroscopic mass, such as Eq. (13), gives different values being applied to the system of two separated nuclei as a whole or separately to each of the nuclei plus their interaction energy. This problem was discussed in Refs. [42,60–63]. The solution suggested there was to take into account a deformation dependence of the nonadditive terms. In particular, according to Ref. [42], the adiabatic potential energy can be calculated as follows:

$$V_{\text{adiab}}(A,Z;\vec{q}) = V_{\text{adiab}}^{\text{standard}}(A,Z;\vec{q}) B(\vec{q})$$
$$+ V_{\text{diab}}(A,Z;\vec{q})[1 - B(\vec{q})], \qquad (17)$$

where $V_{\text{adiab}}^{\text{standard}}$ is the adiabatic potential energy calculated within the standard macro-microscopical approach, and the function $B(\vec{q})$ defines the transition from the properties of two separated nuclei to those of the mononucleus. The function $B(\vec{q})$ should be unity for the ground-state region of the mononucleus and tend to zero for completely separated nuclei. We use the following expression for it: $B(\vec{q}) = \left[1 + \exp\left(\frac{r - R_{\text{contact}}}{a_{\text{diff}}}\right)\right]^{-2}$, where R_{contact} is the distance between mass centers corresponding to the touching nuclei at the contact or scission point, and $a_{\text{diff}} = 0.5$ fm is the adjustable parameter. The procedure of the calculation of the adiabatic potential energy defined by expression (17) was named in

Ref. [42] as the "extended macro-microscopical approach." It leads to the correct adiabatic potential energy in the whole range of nucleus deformation: from the compact ground-state shapes of mononucleus, through a well-deformed configurations of the fission and fusion barriers, up to the system of two separated nuclei.

C. Equations of motion

A rather traditional approach based on the Langevin equations was applied to modeling the time evolution of the nuclear system (see, e.g., reviews [16,34,64] and references therein). The corresponding system of equations is

$$\dot{q}_i = \mu_{ij} p_j, \quad \dot{p}_i = F_i^{\text{driving}} + F_i^{\text{friction}} + F_i^{\text{random}}, \quad (18)$$

where q_i and p_i are the collective degrees of freedom and their conjugate momenta, respectively, m_{ij} is the mass tensor $||\mu_{ij}|| = ||m_{ij}||^{-1}$. As described above, in this model $\vec{q} = \{r, \delta_1, \delta_2, \eta_A, \eta_Z, \varphi_1, \varphi_2, \theta\}$ and $\vec{p} = \{p_r, p_{\delta_1}, p_{\delta_2}, p_{\eta_A}, p_{\eta_Z}, l_1, l_2, l\}$, where $l_{1,2}$ are the angular momenta associated with the self-rotations of the two system parts and l is the angular momentum of relative motion.

The driving, friction, and random forces are calculated as

$$F_i^{\text{driving}} = T \left(\frac{\partial S}{\partial q_i} \right)_{E_{\text{tot}}}, \quad S = 2\sqrt{aE^*},$$

$$F_i^{\text{friction}} = -\sum_{j,k} \gamma_{ij} \mu_{jk} p_k, \quad F_i^{\text{random}} = \sum_j \theta_{ij} \xi_j(t). \quad (19)$$

Here S is the entropy of excited nuclear system, a is the level density parameter [see Eq. (35) below], the excitation energy $E^* = E_{\text{tot}} - V - E_{\text{kin}}$, E_{tot} is the total energy of the system (center-of-mass energy, $E_{\text{c.m.}}$, in our case), $E_{\text{kin}} = \sum_{i,j} \mu_{ij} \frac{p_i p_j}{2}$ is the kinetic energy stored in all the collective degrees of freedom, $\xi_i(t)$ are the normalized random variables with Gaussian distribution $\langle \xi_i(t) \rangle = 0$, $\langle \xi_i(t), \xi_j(t') \rangle = 2\delta_{ij}\delta(t - t')$, and θ_{ij} are the amplitudes of the random force

determined from the Einstein equation $\theta_{ik}\theta_{kj} = \gamma_{ij}T$, $T = \sqrt{E^*/a}$ is the nuclear temperature, and γ_{ij} is the friction tensor.

Since the deformations, charge, and mass asymmetries are finite collective modes, one should use an effective temperature T_i^{eff}, which takes into account quantum fluctuations, instead of the heat-bath temperature T for amplitudes of the random force $\theta_{\delta_i \delta_i}$, $\theta_{\eta_Z \eta_Z}$, and $\theta_{\eta_A \eta_A}$ [65],

$$T_i^{\text{eff}} = \frac{\hbar \omega_i}{2} \coth\left(\frac{\hbar \omega_i}{2T} \right), \quad (20)$$

where ω_i is the frequency with respect to the mode $i = \{\delta_1, \delta_2, \eta_Z, \eta_A\}$. Asymptotically, $T_i^{\text{eff}} \simeq T$ when $T \gg \hbar \omega_i$ and $T_i^{\text{eff}} = \hbar \omega_i / 2$ when $T = 0$. It is clear that the use of the effective temperature instead of the thermodynamic one is extremely important at the first, approaching, stage of nucleus-nucleus collisions, when the temperature T is close to zero. This, in particular, simulates the zero vibrations of the target and the projectile, as well as mass and charge transfer between the yet unexcited reaction partners. The difference in the use of T_i^{eff} and T gradually disappears, when the energy dissipates and the system gets excited. For the charge and the mass asymmetry degrees of freedom, the use of the effective temperature is important even for well-excited systems due to large stiffness coefficients (see Fig. 4) and, thus, large values of $\hbar \omega_{\eta_i}$ (up to several MeV).

Coupling of the deformation degrees of freedom with the relative motion plays a very important role in nuclear dynamics. On the approaching stage, in particular, the main factor determining the variation of the target and projectile deformations is the shift of the minimum of the potential energy towards prolate deformations when the distance between nuclei is getting smaller. Excitation of low-lying vibrational states can be taken into account only approximately due to a continuous character of the Langevin random force not allowing to have a discrete spectra.

Summarizing this subsection, one may write Eqs. (18) for the conjugate momenta in the explicit form (the equations for the collective coordinates are rather trivial)

$$\frac{dp_r}{dt} = -\frac{\partial V}{\partial r} + T^2 \left(\frac{\partial a}{\partial r} \right)_T - \sum_{j,k} \frac{p_j p_k}{2} \frac{\partial \mu_{jk}}{\partial r} + \frac{\hbar^2 l^2}{2\mathfrak{J}_{12}^2} \frac{\partial \mathfrak{J}_{12}}{\partial r} + \sum_{i=1,2} \frac{\hbar^2 l_i^2}{2\mathfrak{J}_i^2} \frac{\partial \mathfrak{J}_i}{\partial r} - \sum_{j,k} \gamma_{rj} \mu_{jk} p_k + \sum_j \theta_{rj} \xi_j,$$

$$\frac{dp_{\delta_1}}{dt} = -\frac{\partial V}{\partial \delta_1} + T^2 \left(\frac{\partial a}{\partial \delta_1} \right)_T - \sum_{j,k} \frac{p_j p_k}{2} \frac{\partial \mu_{jk}}{\partial \delta_1} + \frac{\hbar^2 l^2}{2\mathfrak{J}_{12}^2} \frac{\partial \mathfrak{J}_{12}}{\partial \delta_1} + \sum_{i=1,2} \frac{\hbar^2 l_i^2}{2\mathfrak{J}_i^2} \frac{\partial \mathfrak{J}_i}{\partial \delta_1} - \sum_{j,k} \gamma_{\delta_1 j} \mu_{jk} p_k + \sum_j \theta_{\delta_1 j} \xi_j,$$

$$\frac{dp_{\delta_2}}{dt} = -\frac{\partial V}{\partial \delta_2} + T^2 \left(\frac{\partial a}{\partial \delta_2} \right)_T - \sum_{j,k} \frac{p_j p_k}{2} \frac{\partial \mu_{jk}}{\partial \delta_2} + \frac{\hbar^2 l^2}{2\mathfrak{J}_{12}^2} \frac{\partial \mathfrak{J}_{12}}{\partial \delta_2} + \sum_{i=1,2} \frac{\hbar^2 l_i^2}{2\mathfrak{J}_i^2} \frac{\partial \mathfrak{J}_i}{\partial \delta_2} - \sum_{j,k} \gamma_{\delta_2 j} \mu_{jk} p_k + \sum_j \theta_{\delta_2 j} \xi_j,$$

$$\frac{dp_{\eta_A}}{dt} = -\frac{\partial V}{\partial \eta_A} + T^2 \left(\frac{\partial a}{\partial \eta_A} \right)_T - \sum_{j,k} \frac{p_j p_k}{2} \frac{\partial \mu_{jk}}{\partial \eta_A} + \frac{\hbar^2 l^2}{2\mathfrak{J}_{12}^2} \frac{\partial \mathfrak{J}_{12}}{\partial \eta_A} + \sum_{i=1,2} \frac{\hbar^2 l_i^2}{2\mathfrak{J}_i^2} \frac{\partial \mathfrak{J}_i}{\partial \eta_A} - \sum_{j,k} \gamma_{\eta_A j} \mu_{jk} p_k + \sum_j \theta_{\eta_A j} \xi_j,$$

$$\frac{dp_{\eta_Z}}{dt} = -\frac{\partial V}{\partial \eta_Z} + T^2 \left(\frac{\partial a}{\partial \eta_Z} \right)_T - \gamma_{\eta_Z \eta_Z} \mu_{\eta_Z \eta_Z} p_{\eta_Z} + \theta_{\eta_Z \eta_Z} \xi_{\eta_Z},$$

$$\frac{dl}{dt} \hbar = -\frac{\partial V}{\partial \theta} - \gamma_{\text{tang}} \left(\frac{\hbar l}{\mathfrak{J}_{12}} R_{\text{c.m.}} - \frac{\hbar l_1}{\mathfrak{J}_1} R_{\text{c.m.}}^{(1)} - \frac{\hbar l_2}{\mathfrak{J}_2} R_{\text{c.m.}}^{(2)} \right) R_{\text{c.m.}} + R_{\text{c.m.}} \sqrt{\gamma_{\text{tang}} T} \xi_{\text{tang}},$$

$$\frac{dl_1}{dt}\hbar = -\frac{\partial V}{\partial \varphi_1} + \gamma_{\text{tang}}\left(\frac{\hbar l}{\mathfrak{J}_{12}}R_{\text{c.m.}} - \frac{\hbar l_1}{\mathfrak{J}_1}R^{(1)}_{\text{c.m.}} - \frac{\hbar l_2}{\mathfrak{J}_2}R^{(2)}_{\text{c.m.}}\right)R^{(1)}_{\text{c.m.}} - R^{(1)}_{\text{c.m.}}\sqrt{\gamma_{\text{tang}}T}\xi_{\text{tang}},$$

$$\frac{dl_2}{dt}\hbar = -\frac{\partial V}{\partial \varphi_2} + \gamma_{\text{tang}}\left(\frac{\hbar l}{\mathfrak{J}_{12}}R_{\text{c.m.}} - \frac{\hbar l_1}{\mathfrak{J}_1}R^{(1)}_{\text{c.m.}} - \frac{\hbar l_2}{\mathfrak{J}_2}R^{(2)}_{\text{c.m.}}\right)R^{(2)}_{\text{c.m.}} - R^{(2)}_{\text{c.m.}}\sqrt{\gamma_{\text{tang}}T}\xi_{\text{tang}}. \tag{21}$$

Here indexes j and k run over all the degrees of freedom except for the angular ones ($j,k \neq \theta, \varphi_1, \varphi_2$), $\mathfrak{J}_i$ ($i = 1,2$) are the inertia moments of the system parts assumed to be the rigid-body ones, $\mathfrak{J}_{12} = \mu R^2_{\text{c.m.}}$ is the inertia moment of relative motion, μ is the reduced mass, $R_{\text{c.m.}}$ is the distance between mass centers of the nuclei, and $R^{(i)}_{\text{c.m.}}$ are the distances from the center of mass of the ith nucleus to the central point between the nuclear surfaces. The last three equations in (21) are the same as Eq. (6) in Ref. [19]. It is assumed that the "sliding friction," which is proportional to the relative velocity of the nearest points of nuclear surfaces (expression in the parentheses), is mainly responsible for the so-called dissipation of angular momentum and formation of sticking configuration. For the moment, we do not take into account the derivatives of the potential over the angular degrees of freedom. It is a reasonable approximation for reactions between the nuclei which are spherical in their ground states, when dynamic deformations evolve along internuclear axis $\vec{r}$ (see Fig. 2). The friction coefficient γ_{tang} is taken to be proportional to the radial friction $\gamma_{\text{tang}} = \gamma^0_{\text{tang}}\gamma_{rr}$, where $\gamma^0_{\text{tang}} \simeq 0.1$ is the adjustable parameter.

D. Transport coefficients

The transport coefficients (inertia and friction tensors) play a crucial role in time evolution of a nuclear system. Energy dissipation in mononucleus appears due to viscosity of nuclear "liquid" as a response to a change of its shape ("shape" degrees of freedom are r, δ_1, δ_2, and η_A) and/or oscillation of the neutron subsystem with respect to the proton one (charge asymmetry, η_Z). There is no dissipation of angular momenta (l_1, l_2, and l) at this stage of nuclear reaction, the velocities $\dot{\varphi}_1$, $\dot{\varphi}_2$, and $\dot{\theta}$ are equal to each other and change only due to the variation of the corresponding inertia moments.

The components of inertia tensor m_{ij} corresponding to the shape degrees of freedom are calculated within the Werner-Wheeler approach for incompressible irrotational flow [66]. The surface-plus-window model of one-body dissipation [67] is used for the corresponding components of the friction tensor γ_{ij}. The reduction coefficient of the wall mechanism of energy dissipation is taken to be unity [see, e.g., Eq. (36) in Ref. [34]]. In these models, the inertia and the friction tensors for the shape degrees of freedom are diagonal when nuclei are separated and have ellipsoidal shapes, while the tensors have nonzero off-diagonal components for the mononucleus stage of the system evolution.

The transport coefficients for the charge asymmetry mode (mononucleus stage) are treated in the same way as in Ref. [59]. The inertia coefficient for the charge asymmetry mode is calculated according to Ref. [68] for a flow of viscous incompressible liquid through a cylindrical neck of the radius r_N and the length l_N connecting two spherical parts of the system,

$$m_{\eta_Z\eta_Z} = \frac{m_N}{3\pi\rho}\frac{ZA^2}{N}\frac{(l_N + 2r_N)}{r^2_N}, \tag{22}$$

where ρ is the nucleon density and m_N is a nucleon mass. In order to use this expression, the actual shape of a nucleus is approximated as the two spheres connected by a cylindrical neck in the way of preserving the system mass asymmetry η_A, distance r between centers of the nascent fragments, and neck thickness $r_N = \rho_s(0)$. The friction parameter of the charge asymmetry mode is calculated within the one-body mechanism of nuclear viscosity,

$$\gamma_{\eta_Z\eta_Z} = \frac{4m_N}{9\rho}\frac{AZ}{N}[N\bar{v}_p + Z\bar{v}_n]\frac{1}{\Delta\sigma}, \tag{23}$$

where $\Delta\sigma = \pi r^2_N$ is the neck cross section, and $\bar{v}_p$ and $\bar{v}_n$ are respectively the proton and neutron average velocities inside the nucleus.

The models used in this work to calculate the inertia and friction tensors are essentially macroscopic, which give a high-temperature limit of the transport coefficients. The microscopic effects may be important, for example, on the approaching stage when nuclei just reach the distance where energy dissipation begins. In this region (see below) we use phenomenological friction and inertia form factors having adjustable parameters determined from experimental data. This allows us to avoid an additional model complication assuming that the system may be already enough excited at the contact point to use the macroscopic transport coefficients as a reasonable approximation. At the same time, the microscopic corrections to the transport coefficients (shell effects and influence of pairing, see, e.g., Ref. [69]) and their temperature dependence can be explicitly included into the model in the future.

There are few important peculiarities of treatment of nuclear motion when nuclei are separated. As mentioned above, the inertia and the friction tensors are diagonal in this case. The Werner-Wheeler approach and the model of one-body dissipation can still be used for deformation degrees of freedom δ_1 and δ_2. For relative motion, the inertia coefficient m_{rr} is equal to the system reduced mass. All other transport coefficients $\mu_{\eta_A\eta_A}$, $\mu_{\eta_Z\eta_Z}$, γ_{rr}, $\gamma_{\eta_A\eta_A}$, $\gamma_{\eta_Z\eta_Z}$ are zero for separated nuclei being calculated within the models described above. This does not allow one to take into account the fact that dissipation of angular momentum and energy of relative motion starts already before contact when nuclei approach each other at the distance of nuclear forces range ($\sim$2 fm), and their diffusenesses overlap. There is also a possibility of nucleon transfer at the approaching stage, which can be modeled within the Langevin-type approach in the presence of nonzero transport coefficients only.

In order to take into account these effects and following the surface friction model [16], a phenomenological nuclear friction force with a Woods-Saxon type form factor is included in the model as suggested in Ref. [19]. This additional form factor $F(r)$ tends to zero for the mononucleus stage, where the one-body friction yields a nonzero dissipation. Thus, the radial friction coefficient γ_{rr} is calculated as a weighted sum of two terms,

$$\gamma_{rr} = w_F(r)\gamma_{rr}^{o.b.} + [1 - w_F(r)]\gamma_r^0 F(r),$$

$$F(r) = \left\{1 + \exp\left(\frac{r - R_{\text{contact}} - \Delta R_F}{a_F}\right)\right\}^{-1}, \quad (24)$$

where $\gamma_{rr}^{o.b.}$ is the friction coefficient according to the model of one-body dissipation, and the weighting function is

$$w_F(r) = \left\{1 + \exp\left(\frac{r - R_{\text{contact}} + \Delta R_F}{a_F}\right)\right\}^{-1}. \quad (25)$$

The friction strength γ_r^0, the friction distance ΔR_F, and the friction diffuseness a_F coefficients are the model parameters. Their values can be rather reliably determined by fitting calculations to the experimental data for quasielastic and DI scattering. The most sensitive quantities to these parameters are the grazing angle of the collision, the slope, and the lowest value of the quasielastic part of the fragment energy distribution. The following values were determined in this work: $\gamma_r^0 = 30 \times 10^{-22}$ MeV s fm^{-2}, $\Delta R_F = 2.5$ fm, and $a_F = 0.2$ fm.

It can be shown that the friction coefficients for the mass and charge asymmetries for separated nuclei are related to the corresponding transfer rates as

$$\gamma_{\eta_x \eta_x} = \frac{T}{\lambda_{\eta_x}}, \quad x = A, Z, \quad (26)$$

where the quantity λ_{η_x} can be calculated as [see Eq. (5) in Ref. [19]]

$$\lambda_{\eta_A} = \lambda_A^0 P_{\text{tr}}(r)\frac{4}{A^2}, \quad \lambda_{\eta_Z} = \lambda_Z^0 P_{\text{tr}}(r)\frac{4}{A^2} g_{ZA}, \quad (27)$$

where λ_A^0 and λ_Z^0 are the mass and charge transfer rates, and P_{tr} is the probability of a nucleon transfer depending on the distance between the nuclear surfaces. The term $A^2/4$ appears because the mass asymmetry is used as a collective coordinate. The probability P_{tr} goes exponentially to zero at $r \to \infty$ and equals unity for the overlapping nuclei. In the calculations, we use the semiclassical approximation for $P_{\text{tr}} = \exp(-2\varkappa\xi)$ proposed in Ref. [70]. Here $\xi = r - R_{\text{contact}} - \Delta R_N$, where $\Delta R_N \simeq \Delta R_F$, i.e., the radius of nucleon transfer coincides with the radius of the radial friction and $\varkappa = \sqrt{2\mu_n B_n/\hbar^2}$, where μ_n is the nucleon reduced mass and B_n is its separation energy. Again, for continuity, the friction coefficients for the mass and charge asymmetries for separated nuclei and mononucleus are joined in the vicinity of the contact point. It is assumed that $\lambda_A^0 = \lambda_Z^0$, and the ratio $g_{ZA} = \lambda_{\eta_Z}/\lambda_{\eta_A}$ is the same as given by the corresponding window formulas (close to unity). Thus, we have one free parameter λ_A^0 which was determined by fitting to experimental data on the charge distribution for the ^{136}Xe + ^{209}Bi reaction at $E_{\text{c.m.}} = 569$ MeV
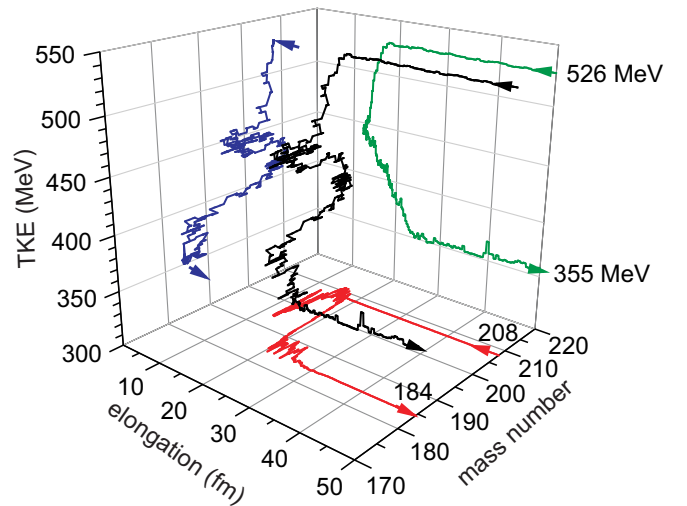
FIG. 5. A trajectory and its projections showing time evolution of energy (potential + relative motion), elongation, and mass of heavier nucleus for the ^{136}Xe + ^{208}Pb combination at $E_{\text{c.m.}} = 526$ MeV.

[see Fig. 6(g) below] to be $1(T/\text{MeV}) \times 10^{22}$ s^{-1}. The corresponding inverse inertia coefficients $\mu_{\eta_A \eta_A}$ and $\mu_{\eta_Z \eta_Z}$ for separated nuclei are estimated assuming that the damping coefficients $\gamma_{\eta_x \eta_x}\mu_{\eta_x \eta_x}$ have the same values as those calculated with the one-body friction and hydrodynamical masses in the vicinity of the contact point. The values of $\mu_{\eta_A \eta_A}$ and $\mu_{\eta_Z \eta_Z}$ are close to each other and equal approximately $0.005 R_0^{-2} m_N^{-1}$.

E. Modeling nucleus-nucleus collisions

Numerical solution of the Langevin equations (18) starts from the approaching stage of collision when the target and projectile are separated by 50 fm and terminates when two reaction products are formed and separated again by approximately 50 fm distance. The solution of these equations is a trajectory in the space of collective coordinates. An example of such the trajectory is shown in Fig. 5, where one may clearly see the energy dissipation process (system heating) as well as mass transfer along with evolution of the elongation degree of freedom. Each trajectory provides full information about a single collision, such as charges and masses of primary (excited) reaction products, their kinetic energies, scattering angles, reaction time, etc. In order to study the characteristics of final fragments we use the statistical model of de-excitation of an excited rotating nucleus described in Sec. II F below.

In this approach, the differential cross sections are calculated in a standard way: (i) a large number of trajectories at different impact parameters $0 < b < b_{\text{max}}$ are simulated; (ii) additional restrictions on the fragment energies, angles, masses, and charges are imposed according to the experimental measurement conditions; (iii) the differential cross sections are then calculated as

$$\frac{d^4\sigma}{dM dZ dE d\Omega}(M, Z, E, \theta)$$

$$= \int_0^{b_{\text{max}}} \frac{\Delta N(b, E, \theta)}{N_{\text{tot}}(b)} \frac{b \, db}{\sin\theta \, \Delta M \, \Delta Z \, \Delta\theta \, \Delta E}, \quad (28)$$

where ΔN is a number of trajectories in specific mass, charge, energy, and angle bins and N_{tot} is the total number of simulated trajectories for each impact parameter. Any single, double, or triple differential cross section can be obtained by integration of Eq. (28).

F. Modeling de-excitation process

One may obtain the characteristics of the primary (excited) reaction products of nucleus-nucleus collisions within the Langevin-type model described above. The de-excitation process can be considered within a statistical model which should be applied separately to each of the fragments. Basic relations of the statistical model used in this paper are given below.

The most important channels of decay of an excited nucleus are evaporation of light particles (neutrons, protons, α's), fission, and γ-quanta emission. The Monte Carlo method is used to obtain the survival probability for all the possible decay channels. At each stage of the decay of the nucleus, one

of the possible events is randomly selected according to their probabilities,

$$P_{\text{b}} = \frac{\Gamma_{\text{b}}}{\Gamma_{\text{tot}}}, \quad b = n, p, \alpha, \gamma, \text{fission},$$

$$\Gamma_{\text{tot}} = \Gamma_{\text{n}} + \Gamma_{\text{p}} + \Gamma_{\alpha} + \Gamma_{\gamma} + \Gamma_{\text{fiss}},$$

where Γ_{tot} is the total decay width calculated as a sum of the decay widths of the considered decay channels. In the case of a particle emission event, its energy e is determined according to the spectra given by the integrand of Eqs. (29) and (30). In the case of fission, the masses and the charges of the fragments are chosen according to the GEF model [71].

Modeling the de-excitation process is terminated either when the nucleus undergoes fission at some stage of decay cascade or when the excitation energy decreases below the fission and the particle emission thresholds and an evaporation residue is formed.
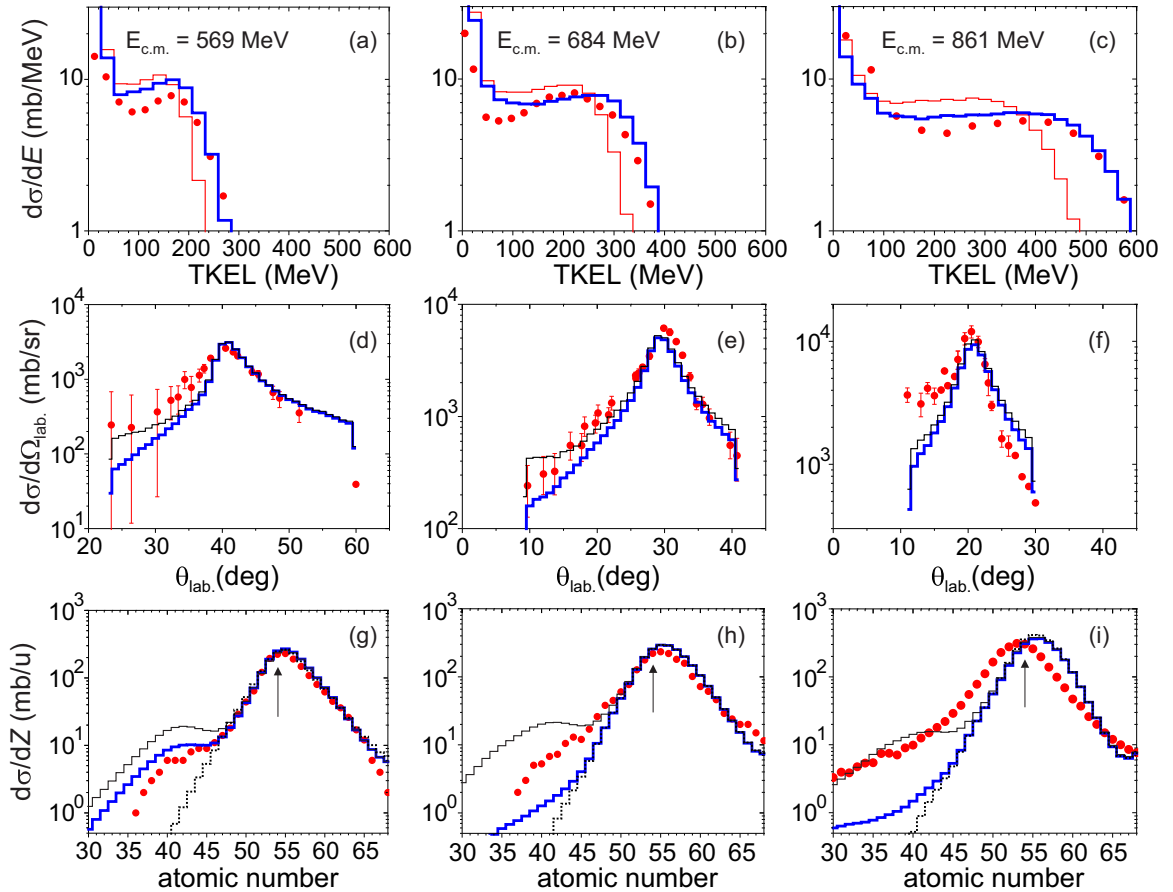
FIG. 6. Comparison of experimental (symbols) and calculated (histograms) energy, angular, and charge distributions for the ^{136}Xe + ^{209}Bi reaction at energies $E_{\text{c.m.}} = 569$ [panels (a), (d), and (g)], 684 [panels (b), (e), and (h)], and 861 [panels (c), (f), and (i)] MeV. The thick solid histograms show the distributions of final fragments with partially eliminated sequential fission events according to the experimental selection criteria. The thin histograms for energy distributions (a), (b), and (c) correspond to the primary fragments. The solid thin histograms in panels (d)–(i) show the distributions of final fragments including all sequential fission events. The dotted histograms are for the final charge yields with completely excluded sequential fission events. Arrows indicate the projectile charge. The experimental data are taken from Refs. [80–82].

The expressions for the particle emission widths have the form

$$\Gamma_{C \to B+b}(E^*, J) = \frac{2s_b + 1}{2\pi \rho_C(E^*, J)} \int_0^{E^* - B_b} \sum_l T_l(e_b)$$
$$\times \sum_{I=|J-l|}^{I=J+l} \rho_B(E^* - B_b - e_b, I) de_b. \tag{29}$$

Here $\rho(E, J)$ is the level density, s_b is the spin of the emitted particle b, and B_b is its binding energy, where $b = n, p, \alpha$; $T_l(e)$ is the probability for the particle to pass through the potential barrier, e_b is the kinetic energy of the emitted particle.

The γ-quantum emission width is

$$\Gamma_\gamma^L(E^*, J) = \frac{1+\kappa}{\rho_C(E^*, J)} \int_0^{E^*} f_L(e_\gamma)$$
$$\times \sum_{I=|J-L|}^{I=J+L} e_\gamma^{2L+1} \rho_C(E^* - e_\gamma, I) de_\gamma, \tag{30}$$

where f_L is the strength function for radiation of multipolarity L and $\kappa = 0.75$ [16,72]. Only the dipole radiation ($L = 1$) is considered.

The fission width is calculated by the expression

$$\Gamma_{\text{fiss}}(E^*, J) = \frac{K_{\text{Kramers}}}{2\pi \rho_C(E^*, J)} \int_0^{E^* - B_{\text{fiss}}} T_{\text{fiss}}(e, J)$$
$$\times \rho_C^{\text{s.p.}}(E^* - B_{\text{fiss}} - e, J) de, \tag{31}$$

where $T_{\text{fiss}}(e, J)$ is the fission barrier penetrability; K_{Kramers} is the Kramers factor [73], and the fission barrier height is calculated as

$$B_{\text{fiss}} = B_{\text{LDM}} + \delta U, \tag{32}$$

where B_{LDM} is the liquid-drop fission barrier [55]; δU is the Strutinsky shell correction to the ground state from Ref. [74].

The level density of the atomic nucleus consisting of Z protons and N neutrons with the total angular momentum J and the excitation energy E^* has the following form

$$\rho(E^*, Z, N, J) = K_{\text{coll}}(E^*, Z, N) \rho_0(E^*, Z, N, J), \tag{33}$$

where $\rho_0(E^*, Z, N, J)$ is the single-particle level density; $K_{\text{coll}}(E^*, Z, N)$ is the enhancement factor which takes into account collective states of the nucleus.

The single-particle level density is calculated according to Ref. [75]:

$$\rho_0(E^*, Z, N, J) = \frac{(2J + 1)a^{1/2}}{24\left(E^* - \Delta - \frac{\hbar^2 J(J+1)}{2\mathfrak{J}_\perp}\right)^2} \left(\frac{\hbar^2}{\mathfrak{J}_\perp}\right)^{3/2}$$
$$\times \exp\left[2\sqrt{a\left(E^* - \Delta - \frac{\hbar^2 J(J+1)}{2\mathfrak{J}_\perp}\right)}\right], \tag{34}$$

where $\mathfrak{J}_\perp$ is the moment of inertia of the nucleus about the axis perpendicular to its axis of symmetry; Δ is the pairing energy,

$$\Delta = \chi \frac{12}{\sqrt{A}},$$

where χ is the parameter equal to 0, 1, and 2 for odd-odd, odd, and even-even nuclei, respectively.

The level-density parameter is [75]

$$a = \tilde{a}\left(1 + \delta U \frac{1 - \exp(-\gamma E^*)}{E^*}\right),$$
$$\tilde{a} = \alpha A + \beta A^{2/3} B_S, \tag{35}$$

where α, β, and γ are the coefficients with the default values 0.073 MeV^{-1}, 0.095 MeV^{-1}, and 0.061 MeV^{-1}, respectively [76]. The functional B_S is the dimensionless quantity equal to the ratio of the surface area of the deformed nucleus with the quadrupole deformation parameter β_2 to that of the spherical nucleus of the same volume. The quantity B_S is calculated for the deformation of the ground state (particle emission widths) and for the saddle point (fission width). Deformations of the nucleus at the saddle point are calculated according to Ref. [77]. The ground-state properties of nuclei (masses, shell corrections, deformations) are taken from Ref. [74]. The ground-state masses for known nuclei are from Ref. [78].

The deformation dependence of the collective enhancement factor K_{coll} is determined according to Ref. [79],

$$K_{\text{coll}}(E^*, Z, N) = K_{\text{rot}}\phi(\beta_2) + K_{\text{vib}}[1 - \phi(\beta_2)],$$
$$K_{\text{rot}} = \frac{\mathfrak{J}_\perp T}{\hbar^2}, \quad K_{\text{vib}} = \exp(kA^{2/3}T^{4/3}), \tag{36}$$
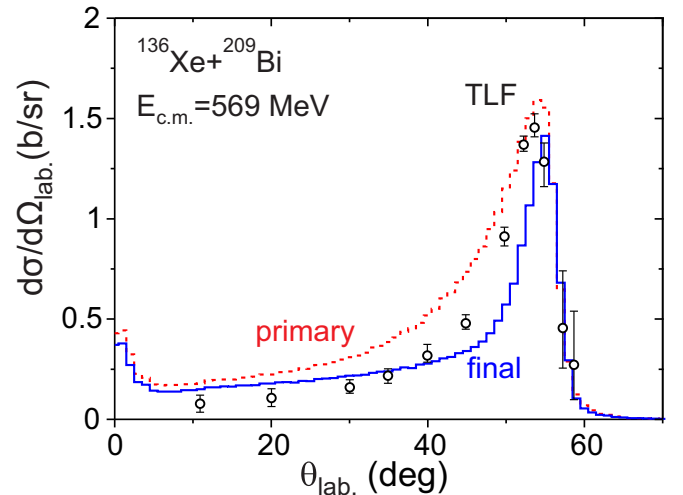
FIG. 7. The angular distribution of Bi-like fragments in the laboratory system for the ^{136}Xe + ^{209}Bi reaction at $E_{\text{c.m.}} = 569$ MeV. The experimental data (symbols) are from Ref. [80]. The calculated distributions (histograms) are for the primary (dashed) and final (solid) fragments. The cross section of the final Bi-like fragments is 33% less than that of the primary fragments due to sequential fission.
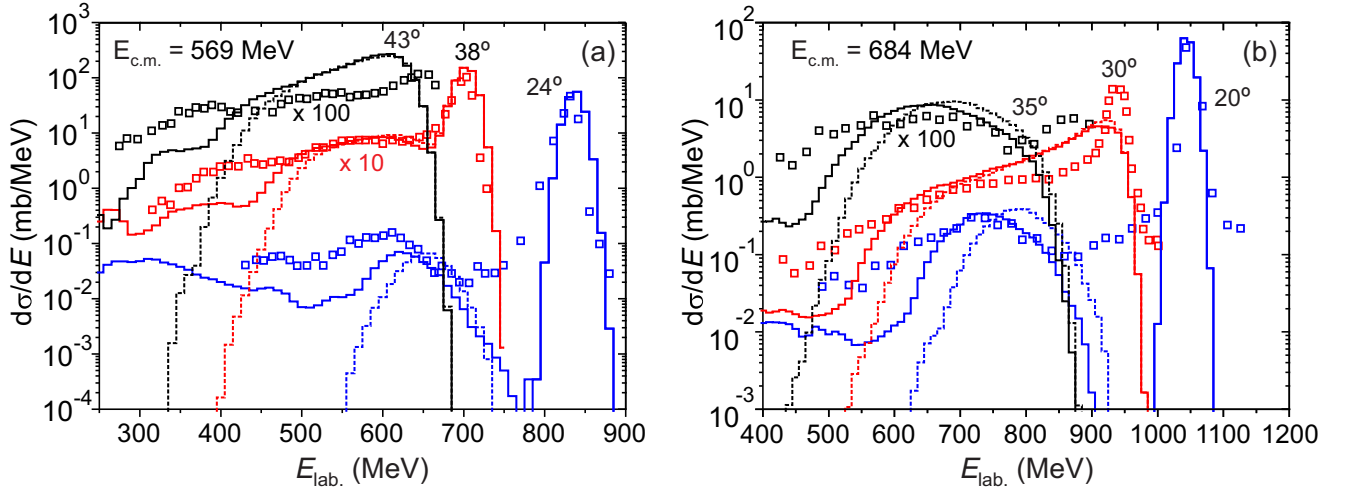
FIG. 8. The laboratory-system energy distributions of the ^{136}Xe + ^{209}Bi reaction products for the indicated angles averaged over 3° bin. The calculation results for primary and final fragments are shown by dotted and solid histograms, respectively. Experimental data (symbols) are taken from Refs. [80,81].

where $k = 0.0555$ [75] and the smoothing function has the form

$$\phi(\beta_2) = \left[1 + \exp\left(\frac{\beta_2^0 - |\beta_2|}{\Delta\beta_2} \right) \right]^{-1}. \quad (37)$$

The default values of the parameters are $\beta_2^0 = 0.15$, $\Delta\beta_2 = 0.04$ [79].

III. ANALYSIS OF MULTINUCLEON TRANSFER REACTIONS

The systems ^{136}Xe + ^{209}Bi, ^{136}Xe + ^{208}Pb, and ^{136}Xe + ^{198}Pt were chosen for the first application of the developed model. First of all, the fusion-fission channel is completely suppressed for such heavy systems. Therefore, one may focus on the analysis of the DI scattering only without overlapping

with other reaction channels. Second, these systems were thoroughly studied experimentally using different methods. Rather complete information was accumulated in the series of experiments conducted for the ^{136}Xe + ^{209}Bi reaction at several energies [80–82]. The ^{136}Xe + ^{208}Pb system was studied recently in Refs. [11,12,14]. Finally, the ^{136}Xe + ^{198}Pt reaction analysis was performed in Ref. [13] aimed at identification of absolute cross sections for products formed in the processes of multinucleon transfer.

A. ^{136}Xe + ^{209}Bi system

The characteristics of the ^{136}Xe + ^{209}Bi reaction were measured at three above-barrier energies $E_{\text{c.m.}} = 569$, 684, and 861 MeV in Refs. [80–82]. Projectilelike fragments (PLFs) were detected in the angular ranges indicated below. The values
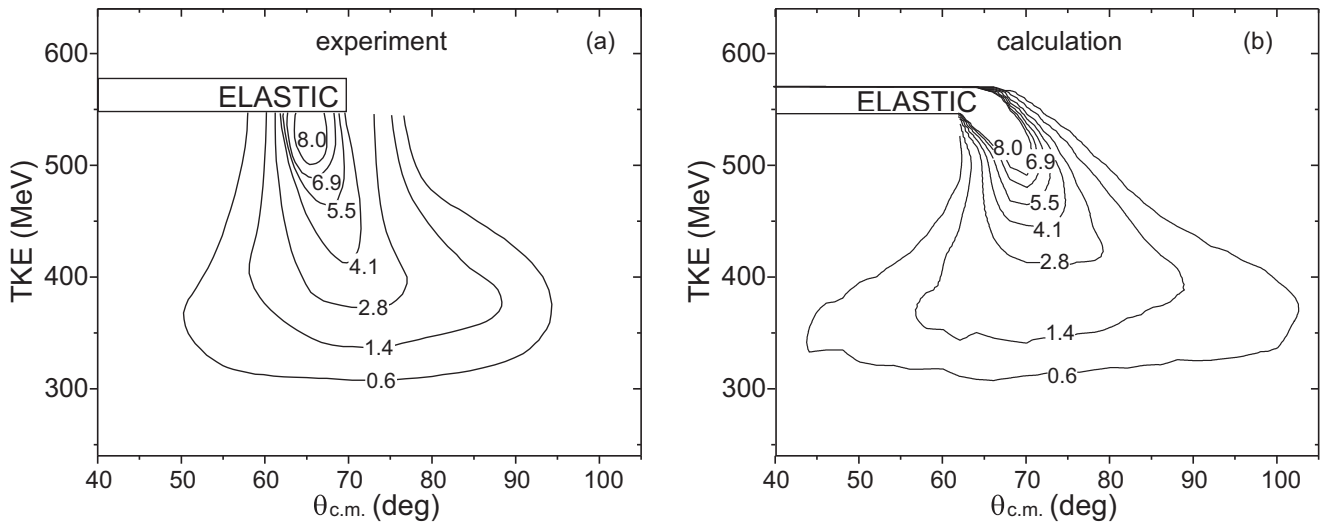
FIG. 9. Experimental [80] (a) and calculated (b) Wilczynski plots $d^2\sigma/dE d\Omega_{\text{c.m.}}$ for the ^{136}Xe + ^{209}Bi reaction at $E_{\text{c.m.}} = 569$ MeV. The cross section is in mb/MeV sr.

of the total kinetic energy loss (TKEL) were restricted in the analysis of the charge and angular distributions, in order to eliminate quasielastic events and events of sequential fission of highly excited targetlike fragments (TLFs). Thus, the following conditions were imposed both on the experimental data and on the calculations: $309 > \text{TKEL} > 23$ MeV and $40° \leqslant \theta_{c.m.} \leqslant 100°$ for $E_{c.m.} = 569$ MeV, $384 > \text{TKEL} > 34$ MeV and $25° \leqslant \theta_{c.m.} \leqslant 75°$ for $E_{c.m.} = 684$ MeV, $601 > \text{TKEL} > 51$ MeV and $18° \leqslant \theta_{c.m.} \leqslant 128°$ for $E_{c.m.} = 861$ MeV. The average experimental charge resolution of three units [full width at half maximum (FWHM)] and 10 MeV

energy uncertainty were taken into account in the calculations as well.

The comparison of the theoretical and the experimental TKEL, angular, and charge distributions of the reaction fragments is shown in Fig. 6. The calculated distributions are in a reasonable agreement with the corresponding experimental data for all the three energies. A rigid shift of the calculated charge distribution with respect to the data for the largest collision energy by two charge units [Fig. 6(i)] should be mentioned. Nucleon transfer in this model is mainly governed by the potential energy. There are positive Q values for the
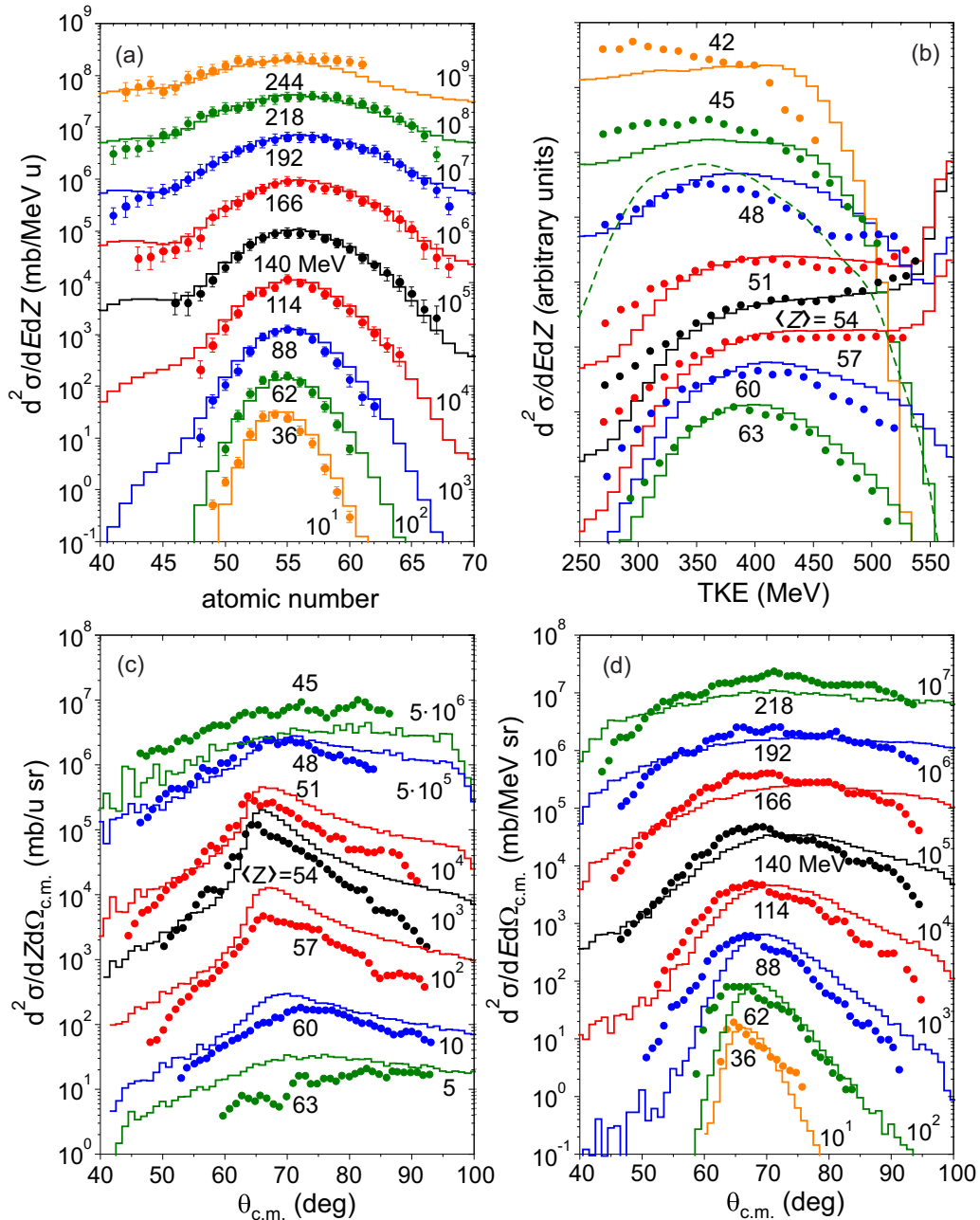
FIG. 10. Sections of the double differential cross sections for the $^{136}\text{Xe} + ^{209}\text{Bi}$ reaction at $E_{c.m.} = 569$ MeV. (a) The charge distributions for different values of TKE; (b) the energy distributions for different Z values; (c),(d) the angular distributions for different Z and TKE values, respectively. The symbols are experimental data [80] and the histograms are calculations for final reaction products. The energy and the charge bins are 26 MeV and three charge units, respectively. The centroids of each bin are shown next to the histograms.

proton transfer from bismuth to xenon. All transfers in the opposite direction are characterized by negative Q values. This results in a larger probability of proton transfer towards symmetrization, namely from target to projectile. This trend is present in the experimental data for the two lower energies as well as in the model calculations for all the three considered energies. The peak of the measured charge distribution for $E_{c.m.} = 861$ MeV is slightly shifted in the direction of lower charges. The origin of this shift is not clear for us.

A noticeably enhanced yields of the light products with $Z < 45$ visible for all the three incident energies is due to contribution of the sequential fission of excited Bi-like fragments, which was not completely eliminated during the analysis of the experimental data [80,81]. In order to simulate the procedure used during the experiment analysis, a detected fragment of sequential fission is treated in the calculations as a product of binary reaction. The assigned TKE value is calculated from the energy and the momentum conservation laws. The charge distributions of the final binary reaction products (without presence of sequential fission) formed after the de-excitation of primary (excited) ones are shown in Fig. 6 by the dotted histograms. The de-excitation process almost does not affect the charges of the fragments, since neutron evaporation dominates. Therefore, the charge distributions of primary and final PLFs of binary reactions practically coincide. The particle evaporation substantially influences, however, the energy distributions, lowering the TKE values. This effect is more pronounced for higher excitation energies, i.e., at larger incident energies and for completely damped events.

The charge and angular distributions shown by thick and thin solid histograms include the sequential fission products. For the former case, the TKEL values are selected according to the experimental procedure, and in the latter case, there is no upper limit for the TKEL values. The TKEL restriction

procedure substantially, but not completely, suppresses the presence of the sequential fission events. It is also seen that the calculated charge distributions should be somewhat wider in order to reproduce the data for the two largest energies. This can be easily achieved by the additional adjustment of the model parameters (inertia coefficients for the charge and/or mass asymmetry for separated nuclei). At the same time, this will worsen the agreement between the calculated and the experimental mass distributions shown in Fig. 12, and especially for numerous isotopic yields discussed below. Therefore, keeping also in mind the uncertainty of treating of sequential fission events, the model parameters were fitted to reproduce better the whole bulk of various experimental observables analyzed in this paper.
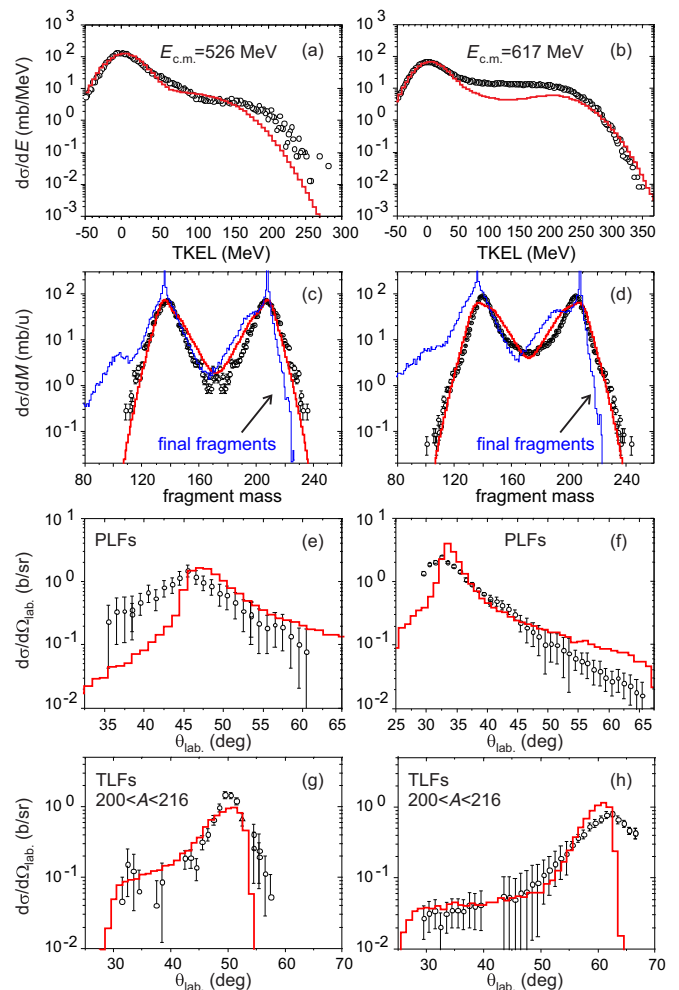
FIG. 12. Energy, mass, and angular distributions of primary fragments for the ^{136}Xe $+$ ^{208}Pb reaction for two collision energies $E_{c.m.} = 526$ MeV [panels (a), (c), (e), and (g)] and $E_{c.m.} = 617$ MeV [panels (b), (d), (f), and (h)]. Experimental data (symbols) are from Ref. [11]. The angular distributions are shown for light reaction fragments ($A \leqslant 172$) and heavy fragments with masses $200 < A < 216$. The thin histograms are the calculated mass distributions of final fragments including the sequential fission events. The original experimental data on the mass distributions are multiplied by 2 in order to obtain the same normalization as for the calculated ones.

FIG. 11. Correlations of the interaction time with number of transferred protons (a), TKEL (b), center-of-mass scattering angle (c), and impact parameter (d) for the ^{136}Xe $+$ ^{209}Bi reaction at $E_{c.m.} = 569$ MeV. The contour lines are drawn over each order of magnitude.

The sequential fission cross section carries important information on the excitation energy of reaction products. It can be estimated from the angular distribution of TLFs. The results of the calculations in comparison with the data are shown in Fig. 7. The sequential fission cross section obtained in this work constitutes 33% of all inelastic events, which is close to the experimentally determined value of 30% [80].

The events of sequential fission also influence the energy distribution of PLFs. Only one of the reaction products was detected in the series of experiments under analysis. Therefore, the sequential fission events were treated as binary ones and then partially eliminated by the TKEL selection discussed above. Since the fragment masses were not measured, the event reconstruction procedure was rather uncertain. This mostly concerns the TKE values and center-of-mass angles. Therefore, it is interesting to analyze the primary experimental data, namely, the measured energy distribution of PLFs in the laboratory frame. Such a comparison is shown in Fig. 8 for the primary reaction fragments (dashed curves) and the final ones including the sequential fission events (solid curves). One may see that the calculations reproduce the position of the quasielastic peak and the maxima of the deep inelastic energy spectra. The sequential fission substantially extends the energy distributions towards lower energies. In spite of in general good agreement with the data, the calculations visibly

differ from them for the largest angles shown. The position of the quasielastic peak, relatively less pronounced in the data, is shifted for $E_{\text{c.m.}} = 569$ MeV, whereas it is absent at all for $E_{\text{c.m.}} = 684$ MeV. These angles are close to the grazing angles, which are $\simeq 44°$ and $32°$ for $E_{\text{c.m.}} = 569$ and 684 MeV, respectively. One may also notice that for the lowest angles the calculated energy distributions have a stronger depression between the quasielastic and the DI events compared with the data. This may indicate that the radial friction at the approaching stage of collision requires further adjustment.

A deeper analysis (compared to that based on the integral characteristics of Fig. 6) of the dynamics of nucleus-nucleus collisions can be made based on various correlation dependencies of the measured quantities. One of such dependencies is the double differential cross section $d^2\sigma/dEd\Omega_{\text{c.m.}}$ known as the Wilczynski plot. It is shown in Fig. 9 for $E_{\text{c.m.}} = 569$ MeV. Four sections of the double differential cross sections $d^2\sigma/dEdZ$, $d^2\sigma/dEd\Omega_{\text{c.m.}}$, and $d^2\sigma/dZd\Omega_{\text{c.m.}}$ of Xe-like fragments are shown in Fig. 10 for the same incident energy. The calculations reproduce the data quite well in the whole range of energies, charges, and angles.

The charge distributions have nearly Gaussian shapes for all the energy-loss bins [Fig. 10(a)]. The width of the distribution increases with increasing energy loss [and, hence, increasing reaction time shown in Fig. 11(a)], whereas the position of
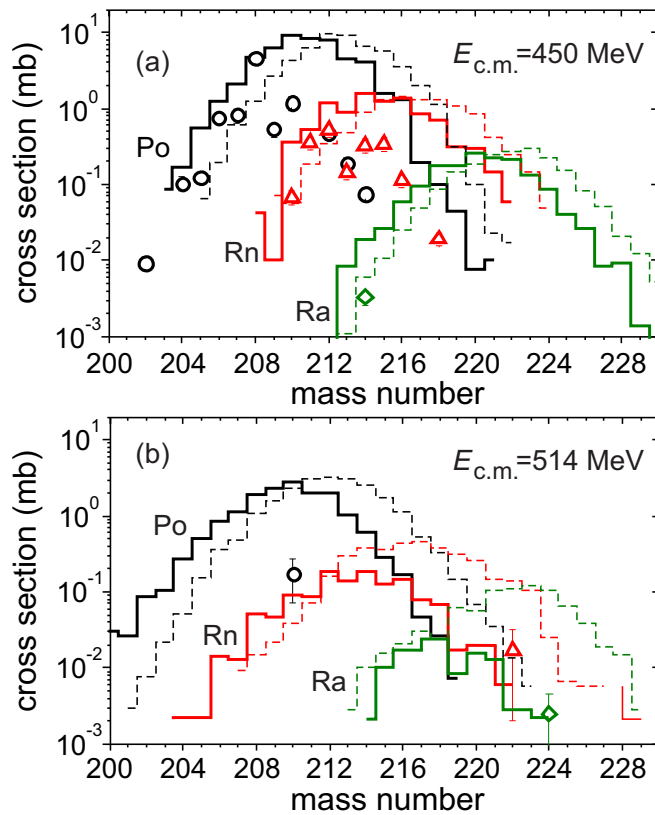
FIG. 13. Calculated primary (dashed histograms) and final (solid histograms) yields of Po, Rn, and Ra isotopes for the ^{136}Xe + ^{208}Pb reaction in comparison with experimental data (circles, triangles, and diamonds for Po, Rn, and Ra, respectively) taken from Ref. [14] for $E_{\text{c.m.}} = 450$ MeV (a) and Ref. [11] for $E_{\text{c.m.}} = 514$ MeV (b).
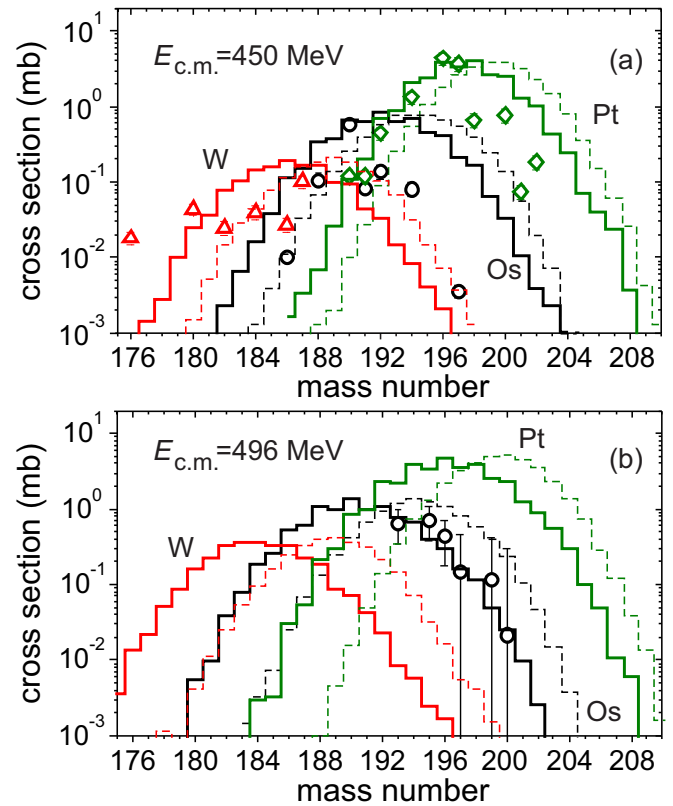
FIG. 14. Same as in Fig. 13 but for W, Os, and Pt isotopes. The data (triangles, circles, and diamonds are for W, Os, and Pt, respectively) are taken from Ref. [14] for $E_{\text{c.m.}} = 450$ MeV (a) and Ref. [12] for $E_{\text{c.m.}} = 496$ MeV (b). The data of Ref. [12] are multiplied by 10 (see the text).

the maximum of the distributions changes only a little. This suggests that the charge distribution for this projectile-target combination is formed with the dominance of the random force (diffusion) over the driving one, in part, owing to the shell effects strongly lowering the potential energy at the positions of the target and the projectile.

The energy distributions [Fig. 10(b)] have a similar behavior for the proton pickup and the proton stripping channels. The quasielastic peak gradually disappears with increasing number of transferred protons, and the shape of the distribution becomes more and more Gaussian-like. It is not completely clear for the lower-charge bins because of the contamination of these bins with sequential fission events. In order to make it more visible, an example of the energy distribution of

the binary fragments is shown for the $Z = 45 \pm 1$ charge bin by the dashed curve. This distribution is rather close in the position of the maximum and the width to the one corresponding to the $Z = 63 \pm 1$ charge bin having the same number of transferred protons. This is correlated with the almost symmetric (with respect to the number of transferred protons) time-charge distribution in Fig. 11(a).

The maxima of the angular distribution shift towards the back angles with increasing energy loss (Fig. 9). This behavior is explained by the correlation of interaction time with TKEL shown in Fig. 11(b). The angular distributions for different energy and charge bins [Figs. 10(c) and 10(d)] become wider and more uniform with increase of the energy loss and with the charge (mass) transfer in the both directions. This indicates
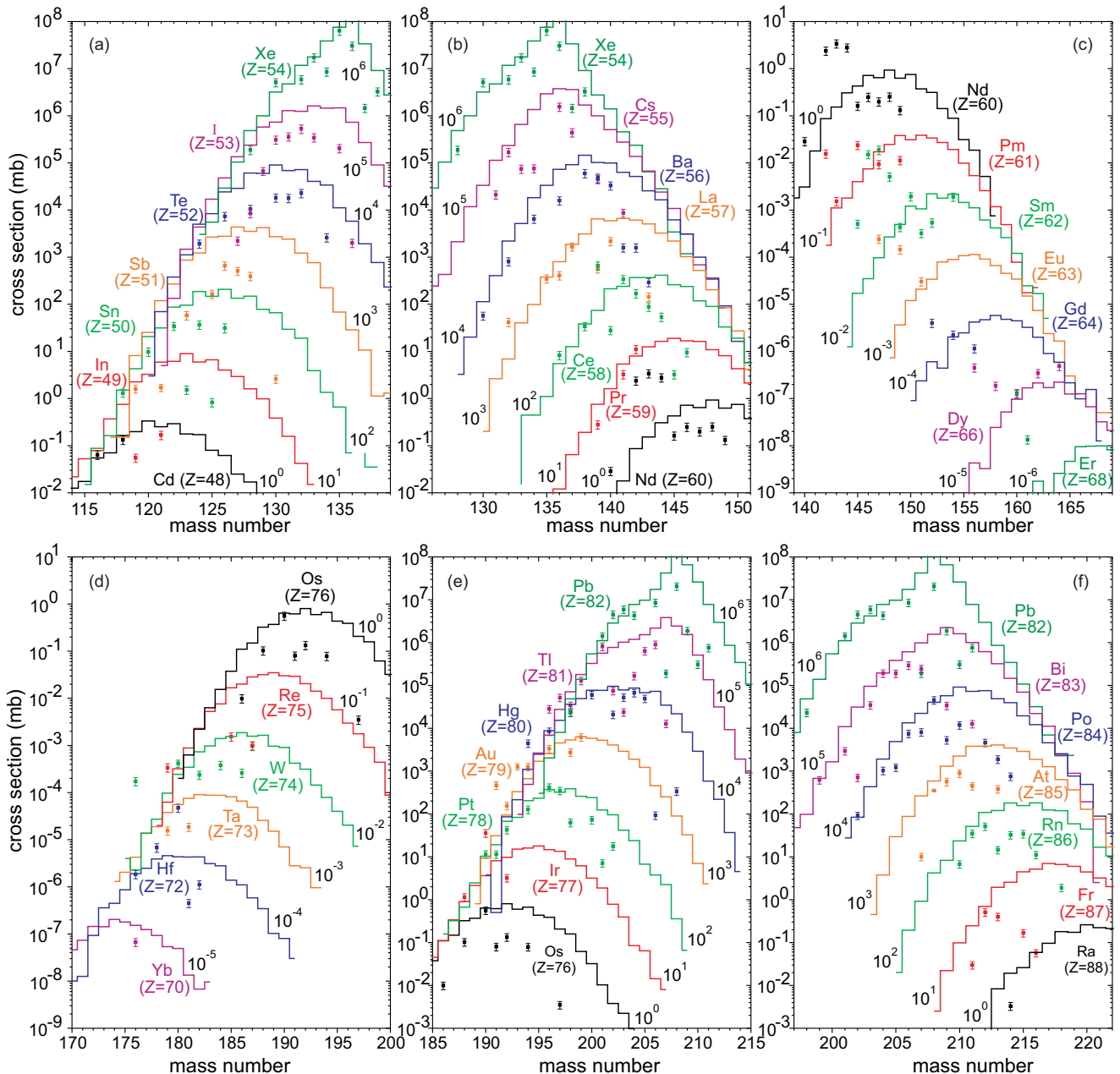
FIG. 15. Comparison of calculated (histograms) and measured [14] (symbols) cross sections for ^{136}Xe + ^{208}Pb at $E_{\text{c.m.}} = 450$ MeV.

that the reaction time increases with the energy loss and charge (mass) transfer [Figs. 11(a) and 11(b)]. The time distribution is wider in the region of smaller charge transfer, and it is getting narrower as the number of transferred protons increases. Therefore, the number of transferred protons cannot be a unique indicator of the reaction time, especially when it concerns the regions around the target and projectile. The same can be concluded about time-angle correlation shown in Fig. 11(c). The widest distribution corresponds to the grazing angle. In contrast, the distribution is rather narrow and peaked at the maximum reaction times in the region of small scattering angles, due to a large time required for the system to make almost a full turn and reseparate at angles smaller than the grazing one. A more straightforward correlation is found between the reaction time and the TKEL. The distribution maintains a rather constant width in the whole range of energy losses, becoming somewhat wider for the completely damped events. Finally, quite evident, but important results are shown in Fig. 11(d): the reaction time is larger for almost central collisions and decreases as the impact parameter grows.

B. ^{136}Xe + ^{208}Pb system

The ^{136}Xe + ^{208}Pb reaction has been studied recently in Ref. [11] at several energies. The covered angular range was $25° \leqslant \theta_{\text{lab.}} \leqslant 70°$. Both reaction products were detected in coincidence using the time-of-flight method. This allowed one to determine the characteristics of the primary (excited) reaction fragments that have survived against sequential fission. The experimental resolution (FWHM) was seven units for the fragment mass and 25 MeV for each of the fragment energies. These experimental conditions and uncertainties are taken into account in the calculations.

Figure 12 shows the comparison of the experimental [11] and calculated energy, mass, and angular distributions for the primary fragments of the ^{136}Xe + ^{208}Pb reaction at two incident energies $E_{\text{c.m.}} = 526$ and 617 MeV. In addition, the total mass yields of final fragments (including the events of sequential fission) are calculated without any restrictions and assuming ideal mass resolution (thin histograms). A good overall agreement with the data is obtained. An evident but not strong underestimation of the maximum value of the TKEL for the lower collision energy contradicts a good agreement of the present calculations with the data of Refs. [80–82] (Fig. 6). This can be the subject of further detailed comparison with the most accurate data on the TKE distributions.

Keeping in mind the primary aim of this paper, namely the analysis of multinucleon transfer reactions as a means of production of heavy neutron-rich nuclei, it is important to compare the calculations with the data not only for the integral mass distributions but also for the independent isotopic yields. Such a comparison is shown in Fig. 13 for the isotopes of Po, Rn, and Ra detected in two independent experiments [11,14] at two rather close collision energies. The data of Ref. [11] were accumulated in angular range $45° \leqslant \theta_{\text{lab.}} \leqslant 55°$, while the entire solid angle was covered in Ref. [14]. The dashed histograms show the primary fragment yields. Since the de-excitation process for $E_{\text{c.m.}} = 450$ MeV proceeds predominantly by neutron evaporation, the final fragment

yields (solid histograms) represent the nearly parallel-shifted primary ones. For the higher collision energy, the excitation is large enough, which leads to a substantial probability of sequential fission for isotopes of radon and radium. The calculations are in a good agreement with the data for proton-enriched nuclei, whereas they distinctly deviate from the data on the neutron-rich side for $E_{\text{c.m.}} = 450$ MeV and reproduce the data for $E_{\text{c.m.}} = 514$ MeV.

An analysis of the production of osmium isotopes in the same projectile-target combination can be made as well. This domain of nuclides is located in the vicinity of $N = 126$. It is this domain that we intend to study. The corresponding experiments were performed at $E_{\text{c.m.}} = 450$ MeV in Ref. [14] and at $E_{\text{c.m.}} = 496$ MeV in Ref. [12]. In the latter case, osmium isotopes having kinetic energies $400 < E(\text{Os}) < 600$ MeV were detected in the angular range $31° \leqslant \theta_{\text{lab.}} \leqslant 54°$. The calculated cross sections are compared with the data in Fig. 14. The data of Ref. [12] are not absolute cross sections but normalized to the theoretical predictions of Ref. [83]. We use an additional normalization factor of 10. Thus, one may compare only the slopes of the calculated and measured cross sections. A good agreement of the calculations with the data for $E_{\text{c.m.}} = 496$ MeV should be noted. As in the case of Po, Rn, and Ra isotopes, overestimation of the cross sections for production of neutron-rich nuclides can be seen for the data of Ref. [14].

In addition, the analysis of all 41 isotopic yields measured in Ref. [14] is shown in Fig. 15 for completeness. As in the previously discussed cases [Figs. 13(a) and 14(a)], the theoretical cross sections are in better agreement with the data on the neutron-deficient side of the mass distribution for each isotope. The measured cross sections on the neutron-rich side are overestimated by the present calculations, especially in the region of masses heavier than the target. It is consistent with the mass distributions shown in Fig. 16. The results of the modeling are very close to the data except for the
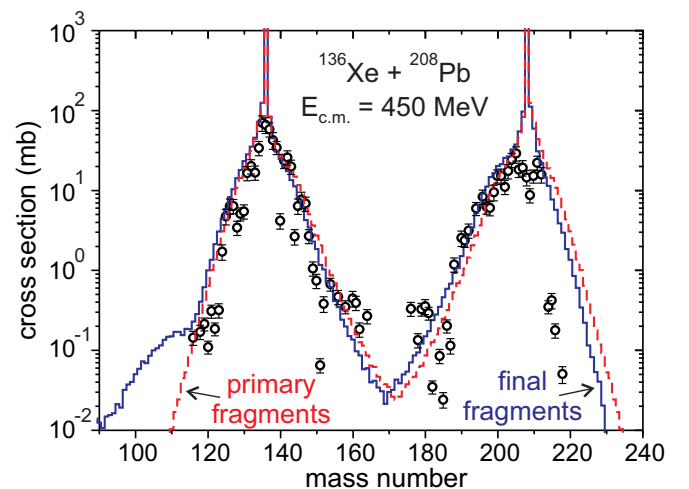
FIG. 16. Mass distribution of reaction products for ^{136}Xe + ^{208}Pb at $E_{\text{c.m.}} = 450$ MeV. The experimental data (symbols) are from Ref. [14]. The solid and dashed histograms are the calculated mass distributions for final and primary fragments, respectively.
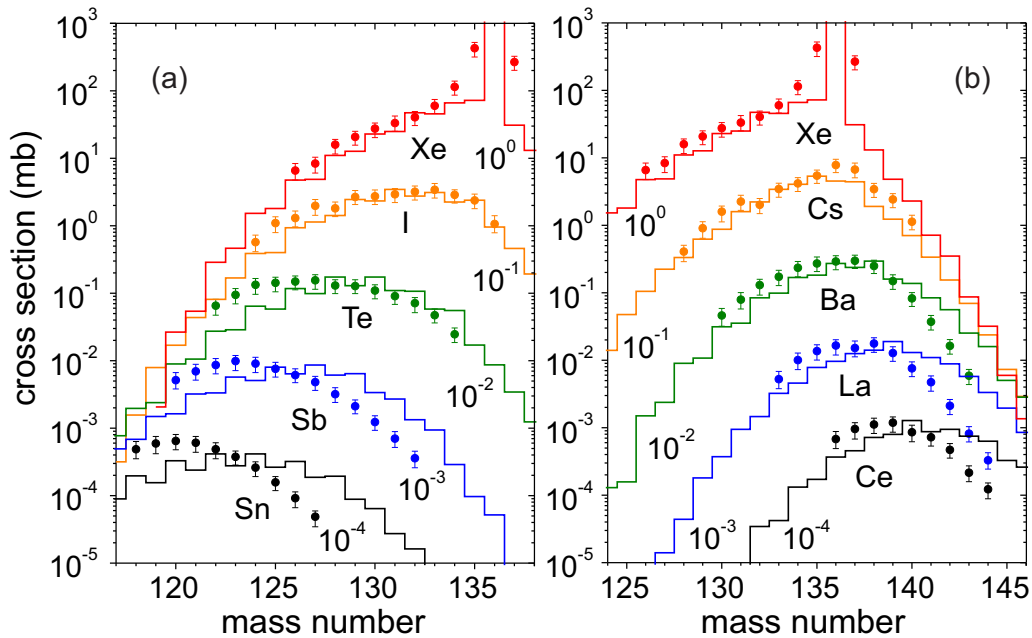
FIG. 17. Calculated (histograms) and experimental [13] (symbols) cross sections of PLFs for the ^{136}Xe $+$ ^{198}Pt reaction at $E_{c.m.} = 643$ MeV.

heaviest masses. At the same time, the calculated cross sections for specific isotopes reasonably agree with the data in all other cases considered in the paper, but corresponding to higher energies, however. In order to reproduce the data on ^{136}Xe $+$ ^{208}Pb at $E_{c.m.} = 450$ MeV, one should change the model parameters responsible for nucleon transfer, e.g., reduce the radius of nucleon transfer. However, this will lead to a strong disagreement with the rest of the data analyzed in the paper. This suggests that additional studies (both theoretical and experimental) are required.

C. ^{136}Xe $+$ ^{198}Pt system

In order to further verify the model, the recent experimental data for the ^{136}Xe $+$ ^{198}Pt system at $E_{c.m.} = 643$ MeV [13] have been analyzed. In the experiment, PLFs have been detected. Cross sections for the corresponding TLFs were then deduced employing an iterative procedure. The results of the analysis are summarized in Fig. 17 for the PLFs and in Fig. 18 for the osmium and mercury isotopes. In the latter case, the data accumulated in different TKEL gates are shown as well. The cross sections are integrated over the experimentally covered angles from 24° to 34°. The calculations reproduce all the data for this system quite well. A shift (maximum of three mass units) of the calculations with respect to the data for the PLFs towards neutron richness is however seen for the channels with the largest number of transferred protons. One may see (Fig. 18) that in this reaction the most neutron-rich nuclei are formed predominantly at low TKEL values, whereas the most proton-rich nuclei are produced in more damped and, thus, more central collisions. This key result for the further discussions coincides with the conclusion made in Ref. [13].

D. Production of neutron-rich nuclides in the vicinity of $N = 126$ shell closure

At this point, it can be concluded that the present model provides a reasonable agreement with various experimental data for a number of studied systems at different collision energies. This provides a basis for the further analysis of synthesis of neutron-rich nuclei in multinucleon transfer reactions. The data on the production cross sections of the $N = 126$ nuclides in the ^{136}Xe $+$ ^{198}Pt, ^{208}Pb reactions are compared with the calculations in Fig. 19(a). One may see a good agreement with the data of Ref. [13] and data on proton-rich nuclei from Ref. [14]. The calculated cross sections for production of neutron-rich nuclei in the ^{136}Xe $+$ ^{208}Pb reaction are strongly overestimated compared with the data of Ref. [14].

According to the calculations, the cross sections for the most neutron-rich nuclei are larger for the ^{136}Xe $+$ ^{198}Pt combination than for the ^{136}Xe $+$ ^{208}Pb one. The difference increases with the increasing neutron richness of a nuclide. The cross sections calculated at two different incident energies for ^{136}Xe $+$ ^{198}Pt are quite close. This encourages further study of the energy dependence of the production cross sections. The results of the corresponding calculations are shown in Fig. 20 for several neutron-rich isotopes with $N = 126$ formed in the ^{136}Xe $+$ ^{198}Pt, ^{208}Pb reactions. One may notice a rather weak dependence of the production cross section of a specific neutron-rich nuclide on the incident energy. The same conclusion was made recently in Ref. [10] based on the dinuclear system model. As already mentioned, the most neutron-rich nucleus with $N = 126$ known at present is ^{202}Os. It can be seen from Fig. 20 that the production cross sections for even more neutron-rich nuclides are relatively high. For example, ^{201}Re and ^{200}W can be
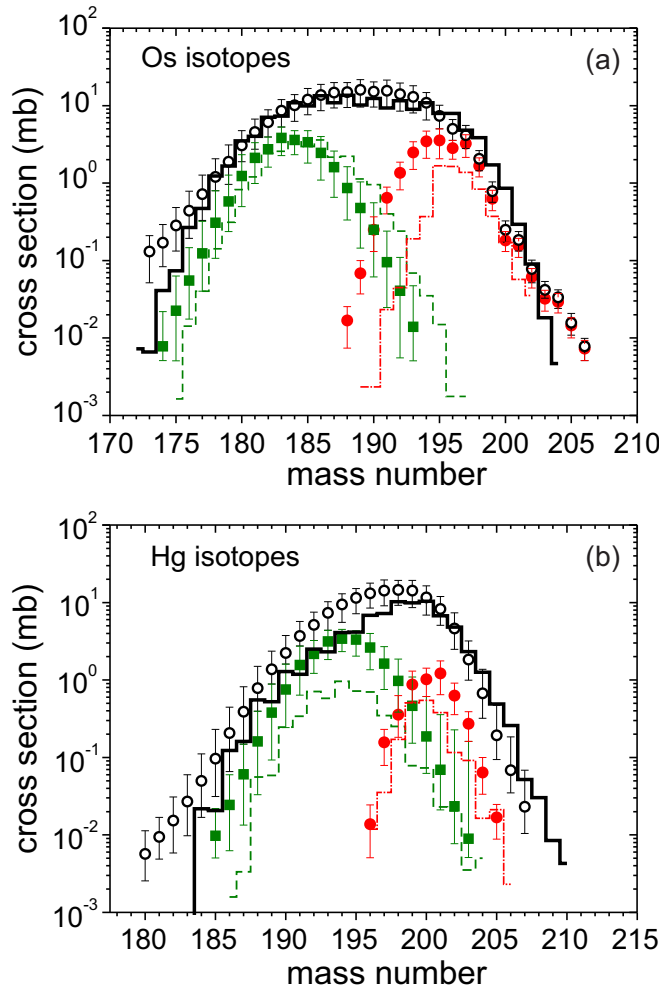
FIG. 18. Cross sections for Os (a) and Hg (b) isotopes integrated over the angular range from 24° to 34° deduced in experiment [13] (open circles) and calculated (solid histograms). Isotopic distributions for different ranges of TKEL from −25 to 25 MeV (dash-dotted histograms and filled circles) and from 175 to 225 MeV (dashed histograms and filled squares) are shown.

FIG. 19. (a) Calculated (histograms) and experimental (symbols) cross sections for production of isotopes with $N = 126$ in reactions ^{136}Xe + ^{198}Pt,^{208}Pb. The solid and dashed histograms are for $E_{c.m.} = 450$ and 643 MeV, respectively. The thin and thick dashed curves are integrated over all angles and over the experimentally covered angles from 24° to 34°, respectively. The experimentally deduced cross sections for the ^{136}Xe + ^{198}Pt system are from Ref. [13] and for ^{136}Xe + ^{208}Pb are from Ref. [14]. (b) Calculated angular distributions in the laboratory frame for the Ir isotopes for the ^{136}Xe + ^{198}Pt,^{208}Pb reactions. The thick histograms are for the ^{203}Ir$_{126}$ nucleus and the thin histograms are integrated over all iridium isotopes. The solid and dashed histograms are for $E_{c.m.} = 450$ and 643 MeV, respectively. The vertical arrows indicate the corresponding grazing angles of TLFs.

synthesized in the ^{136}Xe + ^{198}Pt collisions with the cross sections exceeding 1 μb.

Rather important conclusions can be made regarding the optimal angular ranges for production of neutron-rich nuclei in multinucleon transfer reactions [see Fig. 19(b)]. Whereas the angular distributions are broad being integrated over an isotope mass (iridium in our case), they are much more localized for a specific neutron-rich isotope (the ^{203}Ir$_{126}$ case is shown). The maxima for all the three studied reactions are close to the corresponding angles of grazing collisions. Obviously, the degree of localization depends on the system and the incident energy. The sharpest angular distribution is predicted for the ^{136}Xe + ^{198}Pt system at $E_{c.m.} = 643$ MeV. It is consistent with the calculations of cross sections [compare thick and thin histograms for this system in Fig. 19(a)], as well as the data and calculations in Fig. 18. This figure shows that the cross sections for production of neutron-rich isotopes are almost exhausted by events having low TKEL which correspond to

peripheral collisions. Highly excited transfer products formed in central collisions do not survive. Low values of neutron binding energies enhance this effect. At lower near-barrier energies, even central collisions lead to low excitation energies of primary products (see the difference of the primary and final cross sections shown in Fig. 14 for two collision energies). Moreover, the interaction time increases with the decreasing impact parameter, which favors nucleon transfer. Thus, the angular distributions for neutron-rich nuclides become broader extending towards the forward angles. The most uniform distribution is obtained for the ^{136}Xe + ^{208}Pb combination
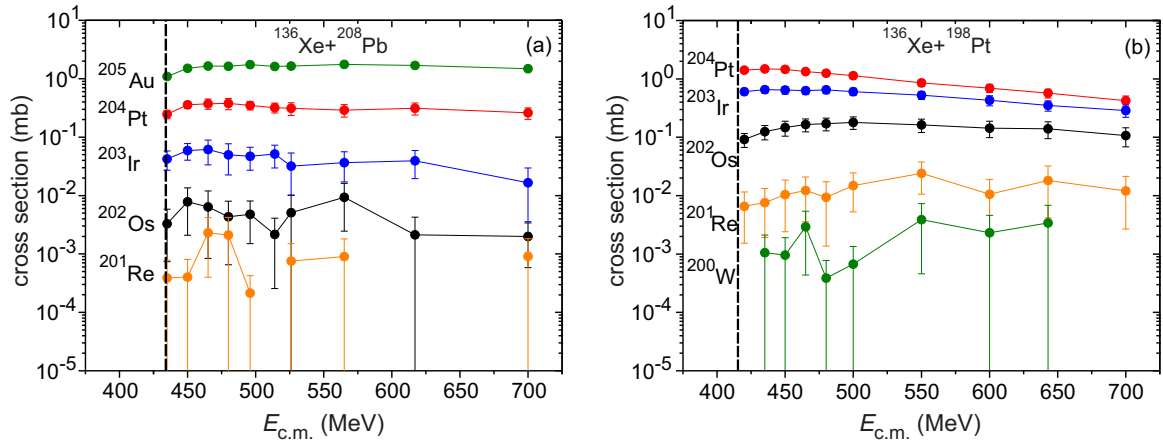
FIG. 20. Energy dependence of the production cross sections of neutron-rich nuclei with $N = 126$ predicted by the present model. The modeling was performed for the ^{136}Xe $+$ ^{208}Pb (a) and ^{136}Xe $+$ ^{198}Pt (b) reactions. The error bars represent statistical uncertainties of the calculated cross sections. The vertical dashed lines show the values of the potential energy at the contact point.

at $E_{c.m.} = 450$ MeV, which can be explained by the lowest difference between the incident energy and the potential energy at the contact point. These peculiarities should be taken into account for designing experimental setups dedicated to studying multinucleon transfer reactions and planning the corresponding experiments.

Figure 21 shows the contour map of the isotope production cross sections in reaction ^{136}Xe $+$ ^{198}Pt ($E_{c.m.} = 643$ MeV). It can be seen that the line corresponding to 100 nb follows the border of the known neutron-rich nuclei over a wide range of atomic numbers. The most neutron-rich nuclides in the $N = 126$ area can be synthesized in this reaction with cross sections exceeding 100 nb, that is more than five orders of magnitude higher than one may expect for the fragmentation reactions used so far.

IV. CONCLUSIONS AND OUTLOOK

In this paper, the multidimensional dynamical model of nucleus-nucleus collisions based on the Langevin equations
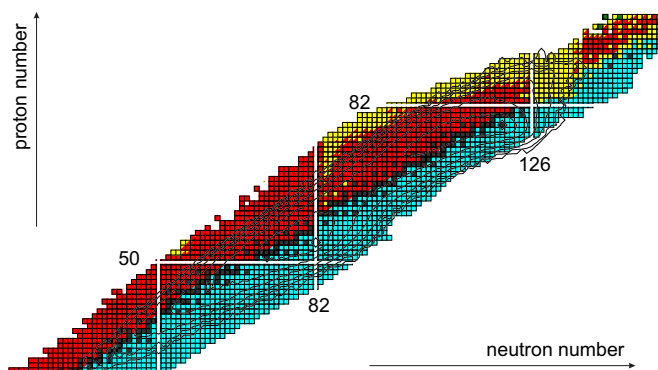
FIG. 21. Upper part of the chart of nuclides. The production cross sections in the ^{136}Xe $+$ ^{198}Pt reaction at $E_{c.m.} = 643$ MeV are shown by contour lines drawn over an order of magnitude of the cross section down to 100 nb.

has been developed. It is combined with a statistical model for simulation of de-excitation of primary reaction fragments. The model provides a continuous description of the system evolution starting from the well-separated target and projectile in the entrance channel of the reaction and up to the formation of final reaction products.

The model showed its applicability to reactions between nuclei, which are spherical in their ground states. It is known that the coupling of the relative motion to the orientation degrees of freedom plays an important role for statically deformed nuclei. Extension of the model for this domain of nuclei is considered as a next step of its development. The most complicated question, which should be solved in this case, is the evolution of axially asymmetric nuclear shapes and the system potential energy in the vicinity of the contact point. It implies, in particular, restoration of the axial symmetry when the interaction time is long enough.

In order to determine the model parameters and test its applicability to deep inelastic reactions, a rather complete set of experimental data available for reactions ^{136}Xe $+$ ^{198}Pt, ^{208}Pb, ^{209}Bi was analyzed. The calculated energy, mass, charge, and angular distributions of reaction products, their various correlations as well as the cross sections for production of different nuclides agree well with the data. On this basis, optimal conditions for detecting the neutron-rich nuclei in the vicinity of the $N = 126$ neutron shell were formulated and the corresponding cross sections were predicted. The yields of neutron-rich nuclei with $N = 126$ are found to be weakly dependent on the incident energy. At the same time, the corresponding angular distributions are strongly sensitive to the reaction dynamics and, thus, the collision energy. They are peaked at grazing angles for larger energies and extend up to the forward angles at low near-barrier collision energies. The corresponding cross sections exceed 100 nb for the nuclei located at the border of the known region, which is nearly five orders of magnitude larger than can be reached in the fragmentation reactions.

This work confirms the earlier-predicted efficiency of multinucleon transfer reactions as a method for synthesis

of neutron-rich nuclei. At the same time, additional high quality experimental data on low-energy nucleus-nucleus collisions with simultaneous measurement of the charges, masses, energies, and angles of reaction products in various mass and energy domains are of a great value for better understanding of the dynamics of nucleus-nucleus collisions at low energies, for adjustment of model parameters as well as for designing the dedicated facilities and planning the corresponding experiments.

[1] S. J. Steer, Zs. Podolyák, S. Pietri, M. Górska, G. F. Farrelly, P. H. Regan, D. Rudolph, A. B. Garnsworthy, R. Hoischen, J. Gerl, H. J. Wollersheim, H. Grawe, K. H. Maier, F. Becker, P. Bednarczyk, L. Cáceres, P. Doornenbal, H. Geissel, J. Grebosz, A. Kelic *et al.*, Int. J. Mod. Phys. E **18**, 1002 (2009).

[2] J. Kurcewicz, F. Farinon, H. Geissel, S. Pietri, C. Nociforo, A. Prochazka, H. Weick, J. S. Winfield, A. Estradé, P. R. P. Allegro, A. Bail, G. Bélier, J. Benlliure, G. Benzoni, M. Bunce, M. Bowry, R. Caballero-Folch, I. Dillmann, A. Evdokimov, J. Gerl *et al.*, Phys. Lett. B **717**, 371 (2012).

[3] A. G. Artukh, G. F. Gridnev, V. L. Mikheev, V. V. Volkov, and J. Wilczynski, Nucl. Phys. A **215**, 91 (1973).

[4] V. V. Volkov, Phys. Rep. **44**, 93 (1978); *Nuclear Reactions of High-Inelastic Transfers* (Energoizdat, Moscow, 1982) (in Russian).

[5] C. H. Dasso, G. Pollarolo, and A. Winther, Phys. Rev. Lett. **73**, 1907 (1994).

[6] R. Broda, J. Phys. G **32**, R151 (2006).

[7] L. Corradi, G. Pollarolo, and S. Szilner, J. of Phys. G **36**, 113101 (2009).

[8] V. I. Zagrebaev and W. Greiner, J. Phys. G **34**, 1 (2007).

[9] V. I. Zagrebaev and W. Greiner, J. Phys. G **35**, 125103 (2007).

[10] Z.-Q. Feng, Phys. Rev. C **95**, 024615 (2017).

[11] E. M. Kozulin, E. Vardaci, G. N. Knyazheva, A. A. Bogachev, S. N. Dmitriev, I. M. Itkis, M. G. Itkis, A. G. Knyazev, T. A. Loktev, K. V. Novikov, E. A. Razinkov, O. V. Rudakov, S. V. Smirnov, W. Trzaska, and V. I. Zagrebaev, Phys. Rev. C **86**, 044611 (2012).

[12] K. Novikov, E. M. Kozulin, I. M. Harca, S. Dmitriev, A. Flueras, P. Greenlees, F. Hanappe, S. V. Khlebnikov, T. Loktev, J. Maurer, A. Di Nitto, J. Pakarinen, P. Ruotsalainen, M. Sandzelius, J. Sorri, M. Sin, W. H. Trzaska, E. Vardaci, and V. I. Zagrebaev, J. Phys.: Conf. Ser. **515**, 012016 (2014).

[13] Y. X. Watanabe, Y. H. Kim, S. C. Jeong, Y. Hirayama, N. Imai, H. Ishiyama, H. S. Jung, H. Miyatake, S. Choi, J. S. Song, E. Clement, G. de France, A. Navin, M. Rejmund, C. Schmitt, G. Pollarolo, L. Corradi, E. Fioretto, D. Montanari, M. Niikura, D. Suzuki, H. Nishibata, and J. Takatsu, Phys. Rev. Lett. **115**, 172503 (2015).

[14] J. S. Barrett, W. Loveland, R. Yanez, S. Zhu, A. D. Ayangeakaa, M. P. Carpenter, J. P. Greene, R. V. F. Janssens, T. Lauritsen, E. A. McCutchan, A. A. Sonzogni, C. J. Chiara, J. L. Harker, and W. B. Walters, Phys. Rev. C **91**, 064615 (2015).

[15] S. Heinz, O. Beliuskina, V. Comas, H. M. Devaraja, C. Heinz, S. Hofmann, E. Kozulin, F. Morherr, G. Münzenberg, D. Ackermann, F. P. Heßberger, B. Kindler, B. Lommel, R. Mann, and J. Maurer, Eur. Phys. J. A **51**, 140 (2015).

[16] P. Fröbrich and I. I. Gontchar, Phys. Rep. **292**, 131 (1998).

[17] Y. Aritomo and M. Ohta, Nucl. Phys. A **744**, 3 (2004).

[18] V. I. Zagrebaev and W. Greiner, Nucl. Phys. A **944**, 257 (2015).

[19] V. I. Zagrebaev and W. Greiner, J. Phys. G **31**, 825 (2005).

[20] K. Hagino, N. Rowley, and A. T. Kruppa, Comput. Phys. Commun. **123**, 143 (1999).

[21] N. V. Antonenko, E. A. Cherepanov, A. K. Nasirov, V. P. Permjakov, and V. V. Volkov, Phys. Lett. B **319**, 425 (1993); G. G. Adamjan, N. V. Antonenko, W. Scheid, and V. V. Volkov, Nucl. Phys. A **627**, 361 (1997).

[22] Z.-Q. Feng, G.-M. Jin, J.-Q. Li, and W. Scheid, Nucl. Phys. A **816**, 33 (2009).

[23] A. K. Nasirov, G. Mandaglio, G. Giardina, A. Sobiczewski, and A. I. Muminov, Phys. Rev. C **84**, 044612 (2011).

[24] J. Aichelin, Phys. Rep. **202**, 233 (1991).

[25] N. Wang, Z. X. Li, and X. Z. Wu, Phys. Rev. C **65**, 064608 (2002); N. Wang and L. Guo, Phys. Lett. B **760**, 236 (2016).

[26] J. L. Tian, X. Z. Wu, K. Zhao, Y. X. Zhang, and Z. X. Li, Phys. Rev. C **77**, 064603 (2008).

[27] C. Li, F. Zhang, J. Li, L. Zhu, J. Tian, N. Wang, and F.-S. Zhang, Phys. Rev. C **93**, 014618 (2016).

[28] A. S. Umar, V. E. Oberacker, and J. A. Maruhn, Eur. Phys. J. A **37**, 245 (2008).

[29] C. Simenel, Eur. Phys. J. A **48**, 152 (2012).

[30] K. Sekizawa and K. Yabana, Phys. Rev. C **88**, 014614 (2013).

[31] A. S. Umar, C. Simenel, and V. E. Oberacker, Phys. Rev. C **89**, 034611 (2014).

[32] A. S. Umar and V. E. Oberacker, Nucl. Phys. A **944**, 238 (2015).

[33] D. Lacroix and S. Ayik, Eur. Phys. J. A **50**, 95 (2014).

[34] G. D. Adeev, A. V. Karpov, P. N. Nadtochy, and D. V. Vanin, Phys. Part. Nucl. **36**, 378 (2005).

[35] V. I. Zagrebaev, V. V. Samarin, and W. Greiner, Phys. Rev. C **75**, 035809 (2007).

[36] V. V. Samarin, Phys. At. Nucl. **78**, 128 (2015); **78**, 861 (2015).

[37] P. A. Cherdantsev and V. E. Marshalkin, Bull. Acad. Sci. USSR **30**, 341 (1966).

[38] U. Mosel, J. Maruhn, and W. Greiner, Phys. Lett. B **34**, 587 (1971).

[39] M. Demeur and G. Reidemeister, Ann. Phys. (Paris) **14/1**, 181 (1966).

[40] P. Holzer, U. Mosel, and W. Greiner, Nucl. Phys. A **138**, 241 (1969).

[41] J. Maruhn and W. Greiner, Z. Phys. A **251**, 431 (1972).

[42] V. Zagrebaev, A. Karpov, Y. Aritomo, M. Naumenko, and W. Greiner, Phys. Part. Nucl. **38**, 469 (2007).

[43] S. Yamaji, H. Hofmann, and R. Samhammer, Nucl. Phys. A **475**, 487 (1988).

[44] W. Scheid, R. Ligensa, and W. Greiner, Phys. Rev. Lett. **21**, 1479 (1968).

[45] W. Greiner, J. Y. Park, and W. Scheid, *Nuclear Molecules* (World Scientific, Singapore, 1995).

[46] A. Diaz-Torres, Phys. Rev. C **69**, 021603 (2004); A. Diaz-Torres and W. Scheid, Nucl. Phys. A **757**, 373 (2005).

[47] G. F. Bertsch, Z. Phys. A **289**, 103 (1978); W. Cassing and W. Nörenberg, Nucl. Phys. A **401**, 467 (1983).

[48] G. R. Satchler and W. G. Love, Phys. Rep. **55**, 183 (1979).

[49] G. G. Adamian, N. V. Antonenko, R. V. Jolos, S. P. Ivanova, and O. I. Melnikova, Int. J. Mod. Phys. E. **5**, 191 (1996).

[50] A. B. Migdal, *Theory of Finite Fermi Systems and Applications to Atomic Nuclei* (Wiley Interscience, New York, 1967).

[51] R. Bass, *Nuclear Reactions with Heavy Ions* (Springer-Verlag, Berlin, 1980).

[52] V. M. Strutinsky, Nucl. Phys. A **95**, 420 (1967); **22**, 1 (1968).

[53] M. Brack, J. Damgaard, A. S. Jensen, H. C. Pauli, V. M. Strutinsky, and C. Y. Wong, Rev. Mod. Phys. **44**, 320 (1972).

[54] H. J. Krappe, J. R. Nix, and A. J. Sierk, Phys. Rev. C **20**, 992 (1979).

[55] A. J. Sierk, Phys. Rev. C **33**, 2039 (1986).

[56] P. Möller, J. R. Nix, W. D. Myers, and W. J. Swiatecki, At. Data Nucl. Data Tables **59**, 185 (1995).

[57] G. D. Adeev, Sov. J. Part. Nucl. **23**, 684 (1992).

[58] J. M. Eisenberg and W. Greiner, *Nuclear Theory, Vol. 1: Nuclear Models* (North-Holland, Amsterdam, 1970).

[59] A. V. Karpov and G. D. Adeev, Phys. At. Nucl. **65**, 1596 (2002); Eur. Phys. J. A **14**, 169 (2002).

[60] W. D. Myers, *Droplet Model of Atomic Nuclei* (FI/Plenum, New York, 1977).

[61] P. Möller, J. R. Nix, and W. J. Swiatecki, Nucl. Phys. A **492**, 349 (1989).

[62] W. D. Myers and W. J. Swiatecki, Nucl. Phys. A **601**, 141 (1996).

[63] P. Möller, A. J. Sierk, and A. Iwamoto, Phys. Rev. Lett. **92**, 072501 (2004).

[64] Y. Abe, S. Ayik, P-G. Reinhard, and E. Suraud, Phys. Rep. **275**, 49 (1996).

[65] L. D. Landau and E. M. Lifshitz, *Statistical Physics. Part 1* (Pergamon, Oxford, 1980).

[66] K. T. R. Davies, A. J. Sierk, and J. R. Nix, Phys. Rev. C **13**, 2385 (1976).

[67] A. J. Sierk and J. R. Nix, Phys. Rev. C **21**, 982 (1980).

[68] E. S. Hernandez, W. D. Myers, J. Randrup, and B. Remaud, Nucl. Phys. A **361**, 483 (1981).

[69] F. A. Ivanyuk, H. Hofmann, V. V. Pashkevich, and S. Yamaji, Phys. Rev. C **55**, 1730 (1997); F. A. Ivanyuk and H. Hofmann, Nucl. Phys. A **657**, 19 (1999).

[70] W. von Oertzen, H. G. Bohlen, B. Gebauer, R. Künkel, F. Pühlhofer, and D. Scühll, Z. Phys. A **326**, 463 (1987).

[71] K.-H. Schmidt, B. Jurado, C. Amouroux, and C. Schmitt, Nucl. Data Sheets **131**, 107 (2016); http://www.khs-erzhausen.de/GEF.html.

[72] V. G. Nedoresov and Yu. N. Ranyuk, *Fotodelenie Yader za Gigantskim Rezonansom* (Naukova Dumka, Kiev, 1989) (in Russian).

[73] H. A. Kramers, Physica (Amsterdam) **7**, 284 (1940).

[74] P. Möller, A. J. Sierk, T. Ichikawa, and H. Sagawa, At. Data Nucl. Data Tables **109-110**, 1 (2016).

[75] A. V. Ignatyuk, *The Statistical Properties of the Excited Atomic Nuclei* (Energoatomizdat, Moscow, 1983) (in Russian), translated as IAEA report INDC(CCP)-233/L, 1985.

[76] A. V. Ignatyuk, M. G. Itkis, V. N. Okolovich, G. N. Smirenkin, and A. S. Tishin, Sov. J. Nucl. Phys. **21**, 612 (1975).

[77] S. Cohen and W. J. Swiatecki, Ann. Phys. **22**, 406 (1963).

[78] M. Wang, G. Audi, A. H. Wapstra, F. G. Kondev, M. MacCormick, X. Xu, and B. Pfeiffer, Chin. Phys. C **36**, 1603 (2012).

[79] V. I. Zagrebaev, Y. Aritomo, M. G. Itkis, Yu. Ts. Oganessian, M. Ohta, Phys. Rev. C **65**, 014607 (2001).

[80] W. W. Wilcke, J. R. Birkelund, A. D. Hoover, J. R. Huizenga, W. U. Schröder, V. E. Viola, K. L. Wolf, and A. C. Mignerey, Phys. Rev. C **22**, 128 (1980).

[81] W. U. Schröder, J. R. Birkelund, J. R. Huizenga, K. L. Wolf, and V. E. Viola, Phys. Rep. **45**, 301 (1978).

[82] H. J. Wollersheim, W. W. Wilcke, J. R. Birkelund, J. R. Huizenga, W. U. Schröder, H. Freiesleben, and D. Hilscher, Phys. Rev. C **24**, 2114 (1981).

[83] V. I. Zagrebaev and W. Greiner, Phys. Rev. Lett. **101**, 122701 (2008).